

2 Article : *Performance benchmarking of microbubble-localization algorithms for ultrasound localization microscopy*

Article accepté pour publication le 29/07/2021 dans *Nature Biomedical Engineering*

Performance benchmarking of microbubble-localization algorithms for ultrasound localization microscopy

Baptiste Heiles^{1,2,*}, Arthur Chavignon^{1,*}, Vincent Hingot^{1,2}, Pauline Lopez^{2,3}, Elliott Teston², Olivier Couture¹

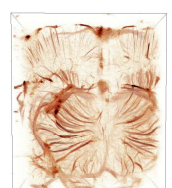
¹Sorbonne Université, CNRS, INSERM, Département Laboratoire d’Imagerie Biomedicale, Paris, France,

²ESPCI, CNRS, INSERM, PhysMedParis, Paris, France,

³Institut Cochin, INSERM U1016, Paris, France,

*Contribution égale de ces auteurs.

Documents complémentaires (figures) accessibles avec la publication à venir.



2.1 Abstract

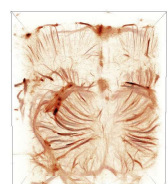
Ultrasound Localisation Microscopy (**ULM**) is an ultrasound imaging technique that relies on the acoustic response of sub-wavelength ultrasound scatterers to map the microcirculation with an order of magnitude increase in resolution as compared to conventional ultrasound imaging. Initially demonstrated *in vitro*, ULM has matured and sees implementation *in vivo* for vascular imaging of organs or tumors in both animal models and humans. The performance of localisation algorithms greatly defines the quality of vascular mapping. In this Resource, we compile a collection of ultrasound localisation algorithms, including two algorithms optimized for reconstruction speed, and compare their performance by proposing eleven metrics, implemented using *in silico* datasets (of simulated canals) and *in vivo* datasets (of a rat brain perfusion, a rat brain bolus, a rat kidney and a mouse tumour). The algorithms, evaluation metrics and datasets are provided in open format as a compendium to setup and perform ULM-based experiments, allowing the user to identify the optimal localisation algorithm for their application, benchmark their own software and enhance the overall quality of their ULM images.

2.2 Main

The circulatory system carries the essential nutrients of life to cells in the body. It forms a 100 000 kilometer-long network composed of centimeter-wide arteries down to capillaries that are a few micrometers in diameter at most. The study of the vascular system is essential for both the diagnosis and treatment of cardiovascular diseases, cancer, diabetes, stroke, or organ dysfunction. Due to its diversity of scale, imaging the vasculature is a daunting task and few techniques are capable of measuring micro-hemodynamics deep in the human body.

Ultrasound imaging is extensively used in medical practice as a non-invasive tool that provides soft-tissue diagnosis, prognosis, or guides interventions. Using the Doppler effect, it can also measure blood flow in real-time. With the advent of plane wave techniques¹, ultrasound has reached frame rates up to 20 kHz making it possible to observe and measure fast occurring changes [1] such as functional changes in the brain [2], as well as increase sensitivity to blood flow that allows more accurate filtering [3,4]. To increase blood's contrast, micrometric gas microbubbles can be intravenously injected *in vivo*. Contrast-Enhanced Ultrasound (**CEUS**) is mostly used for perfusion studies and cardiac imaging [5].

Because conventional ultrasound imaging, Doppler, and contrast-enhanced ultrasound all rely on the propagation of sound waves, ultrasound imaging is largely limited in resolution by diffraction. Recently, Ultrasound Localisation Microscopy (**ULM**) has broken that limit by isolating a small number of microbubbles as subwavelength sources in each image and localizing them with micrometric precision [6–8]. Similar to **PALM** (PhotoActivated Localisation Microscopy), it uses these agents as individual sensors to map the region of imaging by accumulating thousands of events and adding them through density-based methods. When implemented at kilohertz frame rates, ULM can also retrieve the trajectories of microbubbles carried in the bloodstream and reconstruct several centimeters deep, hemodynamic maps of the vasculature both in 2D and 3D [9–11], a feat rising to the challenge of multiscale imaging tools for both the



vasculature and microvasculature. For example, typical imaging of a rat brain with craniectomy *in vivo* with Doppler contrast-enhanced ultrasound and ULM is shown in [fig. 2.1] next to a post mortem microangio-computed tomography (microangio-CT) for reference. Microvessels appear on each modality but sharper and brighter on the ULM rendering (red triangles on [fig. 2.1]).

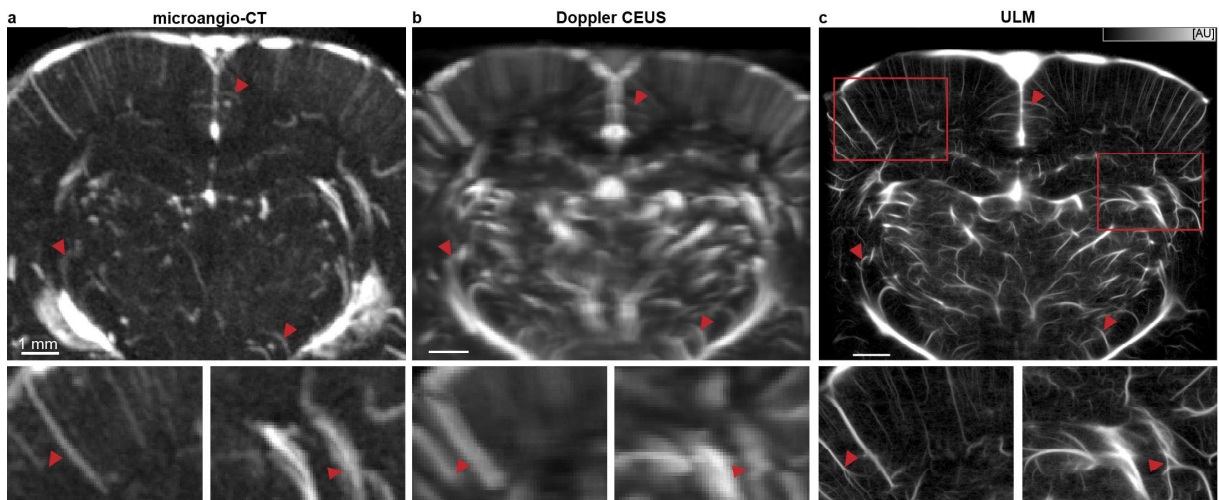
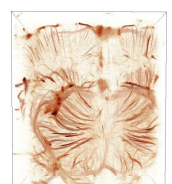


FIGURE 2.1 – Rat brain vascular imaging with *in vivo* ULM and post mortem microangio-CT. **a**, Post mortem microangio-CT with perfusion of μ Angiofil (Fumedica AG, Switzerland) of the rat brain performed with a preclinical micro-CT. Slice of 400 μ m. Red arrows indicate corresponding vessels in the different images. **b**, *In vivo* Doppler contrast-enhanced ultrasound (CEUS) of the rat brain. **c**, *In vivo* ULM of the rat brain with 200 000 images at 1 kHz, red squares indicate where the zooms below each image are taken.

Several teams have been implementing ULM using various localisation techniques over the last few years [6,10,12–14]. The quality of ULM images is directly dependent on the signal-to-noise ratio of the original images or detection filters but most importantly on the localisation and rendering techniques. However, because each team uses different *in vitro* and *in vivo* models as well as different probes, ultrasound machines, and acquisition parameters, comparing these algorithms, along with their general approaches, is difficult. Progress in the field of ultrasound super-resolution is hindered by a lack of widely accepted comparison metrics, even though several attempts have been published on filtering [15], localisation [16–18], and tracking [15] errors.

In this paper, we present a comprehensive open data-processing framework for ULM, including six datasets, *in vitro* and *in vivo* – available at <http://doi.org/10.5281/zenodo.4343435> – complemented by a series of universal performance metrics to evaluate quantitatively different ULM implementations. We provide five of the most used algorithms for microbubble localisation to compare their performances : Lanczos, spline and cubic interpolation (**Lz-Interp**, **Sp-Interp**, **Cub-Interp**), Gaussian fitting of the PSF (**Gauss-Fit**), and a no-shift method that assumes ideal centering of the microbubble in the pixel. The scripts along with our Localisation and tracking Toolbox for Ultrasound Super-resolution (LOTUS), are available on a GitHub repository (<https://github.com/AChavignon/PALA>). In Supplementary figure 6-1, we have compiled the localisation methods used and their related articles as well as a few comments.

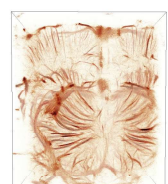


Localisation method	Related articles	Comments
Gaussian fitting	(Ackermann and Schmitz, 2016 ; Luke et al., 2016 ; O'Reilly and Hynynen, 2013 ; Song et al., 2018b) [19–22]	Usually, these works use a Gaussian convolved PSF rather than a Gaussian fitting with an optimizer.
Weighted average based	(Christensen-Jeffries et al., 2015 ; Hansen et al., 2016 ; Heiles et al., 2019 ; Lin et al., 2017 ; Song et al., 2018a ; Souldioti et al., 2018 ; Viessmann et al., 2013 ; Zhang et al., 2018 ; Zhu et al., 2019) [10,13,15,23–28]	Except for Heiles et al 2019, these work on data beamformed with pixels of sizes below the wavelength or data beamformed with commercial scanners which might affect PSF shape and full width at half maximum.
Lanczos based interpolation and Gaussian fitting	(Errico et al, 2015) [9]	
Spline based interpolation	(Huang et al., 2020 ; Song et al., 2018b) [22,29]	
Linear based interpolation	(Song et al., 2018a) [15]	On top of the linear-based interpolation, this paper convolves with a Gaussian profile.
Cubic based interpolation	(Song et al., 2018b) [22]	This paper is a comparison of algorithms
Radial symmetry	(Parthasarathy, 2012) [30] (optic super-resolution only)	
RF-based	(Brown et al., 2019 ; Christensen-Jeffries et al., 2017a, 2017b ; Desailly et al., 2013, 2015) [16,17,31–33]	These papers are based on radiofrequency data before beamforming. In particular, the papers from the team at Imperial College/Kings College London use the onset of the Hilbert transform of the RF signals.

In addition, we introduce two algorithms developed by our team called weighted average (**WA**) and radial symmetry (**RS**). We provide all algorithms ready for use so that labs lacking the expertise to implement ULM can contribute to the fast development of ultrasound super-resolution imaging (see supplemental data). Importantly, we introduce metrics that address still unanswered questions such as : how accurate and sensitive is the localisation algorithm [17], how much is ULM affected by low SNR [13], what affects the precision of the code, how well is it possible to reconstruct difficult structures such as highly tortuous vessels, aneurysms, stenosis, where do the grid artifacts come from [34], and finally how can 3D ULM be implemented without a dramatic increase in computational power and time? The platform is designed to allow the integration of new metrics and answers to questions the user might come up with on its own.

2.3 Results

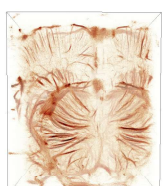
Ultrasound localisation microscopy is a multi-step process comprising the acquisition of a large number of frames, pre-processing, detection, localisation, and image reconstruction as described in [fig. 2.2] and Supplementary Figure 1-1. Although this article is mostly focused



on the comparison of localisation algorithms, readers will find, in supplementary material, the scripts and appropriate open software (LOTUS) to perform each of these steps in the most straightforward way. These scripts can be easily adapted to different acquisition types or various computer setups and parallelized. In LOTUS, users can load their own acquired data, filter it, localize microbubbles, track them and generate ultrasound super-resolution renderings.

2.3.1 *In silico* and *in vivo* datasets

To study the performances of different localisation algorithms, the first step was to create and acquire 3 different datasets, each of which we make fully available for reuse in supplementary materials. The first one ("*in silico* PSF"), the point-spread function (**PSF**) simulation, is designed to study non-uniformity effects on localisation and spatial sampling effect on the beamforming process. It consists of a point-like scatterer moved in a $\lambda \times \lambda$ space, the size of one pixel, by $\lambda/21$ steps, resulting in 441 positions. The second dataset ("*in silico* Flow"), the microcirculation simulation, allows for testing *in silico* more fundamental aspects of resolution such as the separability of microvessels and the accuracy of microbubble tracking. It is comprised of complex 3D tubes in the imaging plane mimicking an actual 2D imaging situation. Inside, point-like scatterers are placed at random in each of the tubes section and then are propagated through 20 000 frames according to a Poiseuille flow model assuming continuity on streamlines. Concentrations, speeds, and noise level can all be modified by the user and are presented in the methods section 2.7. The maximum velocities in each of these tubes range from $0,05\lambda/\text{frame}$ to $3\lambda/\text{frame}$. We studied the localisation errors and the effect of different signal-to-noise ratios (SNR) using this dataset. For these datasets, the point-like scatterer's ultrasound response is simulated using the Verasonics Research Ultrasound Simulator (Verasonics Inc., Kirkland Washington, USA), using a 128 elements linear probe, with elements' pitch at a wavelength ($\lambda = 100 \mu\text{m}$).



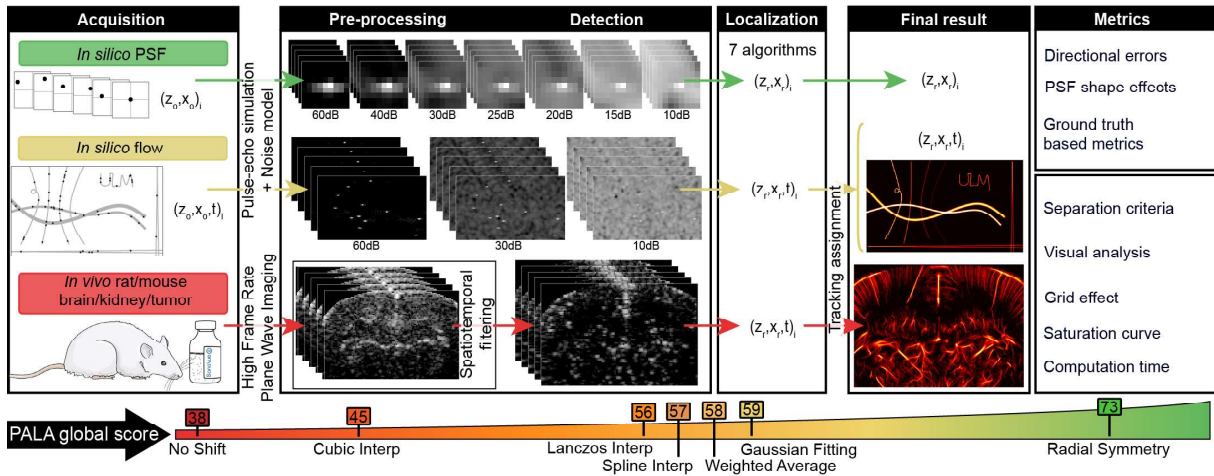


FIGURE 2.2 – Description of the framework for data simulation and performance assessment. The framework presented here fits easily into the classical layout of ULM acquisition, filtering/pre-processing, detection of microbubbles, localisation of events' centers, tracking, and mapping of the flow. Each dataset gives different information about the localisation process. The separation criteria, which defines maximum resolution attainable is given by dataset "*in silico* PSF". The ground truth based metrics are given by *in silico* datasets. *In vivo* datasets, "*in vivo* rat brain perfusion", "*in vivo* rat brain bolus", "*in vivo* rat kidney", "*in vivo* mouse tumor", give information about the *in vivo* visual aspect, the influence of the algorithms on the grid effect and on computation time. Visual analysis is also provided by dataset "*in silico* Flow". The PALA global score is calculated based on a combination of the metrics on the right column computed on *in vivo* and *in silico* datasets. By summing and weighting each of these metrics derived scores, we obtain the global score, designed to grade the algorithms' performance.

While the simulation-based datasets give access to the ground truth and are useful to compare the error of localisation-based metrics, the best validation is still *in vivo* experiments as we are confronted with multi-factorial signal noise, breathing motion, speed of sound changes coming from propagation through fatty tissue, pulsating blood and other phenomena arduous to reproduce in simulation. Imaging different organs allow us to compare different physiologies, hemodynamics, and anatomical geometries. The *in vivo* datasets comprise of :

- "*in vivo* rat brain perfusion", "*in vivo* rat brain bolus" : two Sprague Dawley rat brains at different coronal sections. One was acquired while continuously injecting microbubbles through the jugular vein (192 000 ultrasound images at a SNR of 29 dB), another one by injecting a bolus of microbubbles in the caudal vein (170 000 frames at a SNR of 28 dB).
- "*in vivo* rat kidney" : a Sprague Dawley rat kidney (188 020 frames at a SNR of 26 dB)
- "*in vivo* mouse tumor" : A subcutaneous tumor implanted in an FvB strain mouse (30 000 frames at a SNR of 25 dB)

The *in vivo* angiography of the rat brain with continuous injection is named "*in vivo* rat brain", which is the most complete dataset and one that has already been used as reference [8,35]. The skull of the rat was previously removed following craniotomy surgery protocol (detailed in the Methods section). The other rat brain we imaged went through the same protocol with a different method for injection. The rat kidney dataset was acquired after isolation of the



kidney outside of the rat following lumbotomy protocol (detailed in Online methods). The tumor dataset was obtained on a subcutaneous tumor in mice after implantation of primary cancerous cells developed in mouse mammary tumor virus-polyoma middle tumor-antigen (MMTV-PyMT) donor mice (detailed in Online methods). The kidney and mouse tumor datasets are more subject to breathing motion than the rat brain since the animal is not fixed. These datasets will thus allow us to compare the performance of the algorithms in low SNR, moderate motion situations. The mouse tumor which is expected to have a disorganized vasculature is of particular interest.

On each of these datasets, and based on the state of the art we selected and applied 7 different localisation algorithms to retrieve subwavelength positions. They are then processed by a Kuhn-Munkres assignment to perform tracking and velocimetry [36,37]. Final images are reconstructed by density projection or velocity renderings. The whole framework is presented in [fig. 2.2].

2.3.2 General comparisons of 7 algorithms using 11 metrics

To alleviate the current difficulty in comparing the attainable resolution in different organs and by different groups, we report here 11 different metrics to compare various ULM algorithms. In each simulated dataset, we look at the directional errors, statistical measures using a binary classification test, and separation criteria to define maximum attainable resolution. For *in vivo* results, we report an in-depth visual analysis as well as grid effect characterisation, and computation time. In the end, the localisation algorithms are rated with an overall scoring called PALA global score that takes into account errors, the ability to detect microbubbles accurately, and computation time, computed on *in silico* and *in vivo* datasets (see Methods section 2.7 and Supplementary Figure 5-1 to 5-4). The results are presented in [fig. 2.3].

Two algorithms, Gaussian fitting, and radial symmetry come out on top on almost every quantitative index that we have devised. However, when looking at the time it takes to perform ULM with tracking and localisation, the ranking is modified. The weighted average and the radial symmetry-based algorithms are the fastest localisation implementations, while the Gaussian fitting is almost 50 times slower. The values presented in [fig. 2.3b] were normalized according to the fastest implementation which takes for the *in vivo* dataset around 3 minutes, faster than the actual acquisition of the images.



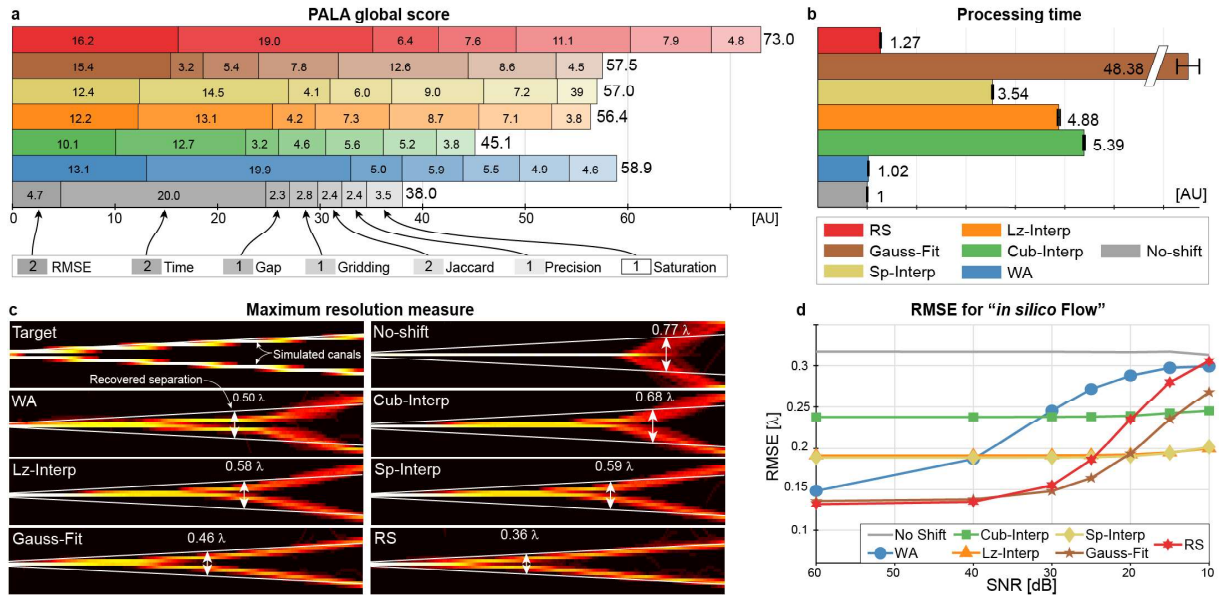


FIGURE 2.3 – Results of the study combined in the PALA global score for each algorithm. **a**, PALA global score obtained with the different scores from "in silico PSF" dataset : RMSE, "in silico flow" dataset : minimum separation measured between the two canals (i.e. maximum resolution), Jaccard index, precision value, and "in vivo" rat brain perfusion : the time factor, gridding index and saturation index based on saturation curves (see [fig. 2.7]). The bigger the score, the higher is the performance of the algorithm. To reflect the importance of the different indices, some of them were multiplied by coefficients (value in legend). These arbitrary coefficients allow us to double the impact of RMSE, time factor, and Jaccard index, the three indices we consider most critical. The weights used as well as the exact formulae for the conversion of the metrics to arbitrary unit scores on a scale of 0 to 100 are available in the methods section 2.7 and a supplementary dynamic table "PALA_GlobalScores_DynamicTable.xlsx". Different weights have also been chosen to reflect implementations where time or SNR influence might be less crucial in the supplementary information. **b**, Computation time for each algorithm compared to the fastest implementation, the no-shift implementation taking 3 minutes on our high-end computer (Intel Core i9 @ 2.9 GHz 12 cores, NVidia RTX 2080Ti, 128 GB RAM @ 2133 MHz). Error bars represent $\pm s.d.$. ($N = 240$ blocks of 800 frames). **c**, Maximum resolution attainable on the dataset "in silico Flow" at SNR = 30 dB with different localisation schemes. λ represents the wavelength. For each rendering, the point where the intensities of the two canals reconstructed are distinct by more than 3 % is calculated. The lateral position at which it is located is taken to calculate the real distance between the two simulated canals. That is taken as the minimum separation that can be accurately recovered by the algorithm. It is the separation index. **d**, Root mean square error of the localisation schemes for recovery of simulated points in dataset "in silico Flow" with different SNR.

Overall the radial symmetry (RS) based and weighted average (WA) algorithms showed the highest performance with the weights chosen. Looking closer, the maximum resolution attainable measured as the separation criteria is the highest for the RS and Gauss-Fit based algorithms at 0.36λ and 0.46λ . The time factor, however, is the lowest for the WA with under 3 minutes of calculation which is lower than the acquisition time with our computer. The large increase and very low root mean square error (RMSE) minimum of the weighted average algorithm (0.13λ) confirm that it is a very good candidate for localisation at a high signal-to-noise ratio (SNR).



but that one should switch to either **Gauss-Fit** or **RS** when the SNR worsens below 30 dB. At 15 dB and downwards, one should theoretically consider using interpolation-based algorithms (see Supplementary Figures 3-3). The gridding index, which is a quantitative measure of the reprojection of localized microbubbles on the original beamformed grid, impairing accurate vessel delineation, is maximized for both **RS** and **Gauss-Fit** approaches. This gridding index increases when specific spatial frequencies are overexpressed.

2.3.3 Accuracy metrics in simulated datasets

We simulated both *in silico* datasets with 7 different signal-to-noise ratios from 10 dB to 60 dB (white Gaussian noise model, 0,2 ohm impedance noise, ± 10 dB amplitude, for clutter filtered with 0,7 pixel wide 2D Gaussian kernel, see Supplementary figure 2-3). The different localisations in the 30 dB set were classified depending on their distance to the scatterer simulated position. When this distance is lower than $\lambda/4$, the localisation is deemed successful, otherwise, it is either classified as a false negative (FN) if an existing scatterer was not detected or as a false positive if no real scatterer was present (FP) (see [fig. 2.4a], and Supplementary Figure 3-6). The highest number of localisations 386 000, calculated as the total of false and true positives is obtained in the radial symmetry case, with 12 % more than the worst-rated algorithm, the **Cub-Interp**. The number of true positives is the highest in the **Gauss-Fit**/RS-based algorithms with a value of 3,7 and 3,5 times higher respectively than the no-shift algorithm. The interpolation-based algorithms have similar TP values while the cubic interpolation fares the worst. The same trends in FP and FN numbers can be observed. To interpret these more easily, the precision, Jaccard, and sensitivity indices were also plotted [fig. 2.4b]. For the three indices, the **Gauss-Fit** and **RS** come out on top with as much as 85,9 % simulated scatterers being picked up by the best localisation algorithm.

The sensitivities of **WA** and the best interpolation-based algorithms are quite low at around 40 %, while the precision is higher for the latter at 71,8 % [fig. 2.4b]. The no-shift algorithm has the lowest values albeit not as low as one would expect given that no localisation is involved. The Jaccard index which represents a detection rate is at most 63,2 % and can be as low as 11,8 % for the no-shift scheme. **Gauss-Fit** and **RS** are more precise than others. This is due to a low localisation error, and as such a high cardinality of true positives. As the total number of TP+FN is finite, this also means that the sensitivity index is high. For the weighted average scheme, we measure a high precision and high sensitivity although its localisation error is the highest among the schemes. It gives us a glimpse into why this happens : the TP and FN values are almost identical to the best interpolation schemes.

The directional errors are calculated for every simulated point and every recovered localisation [fig. 2.4c]. At first look, **WA** and **Cub-Interp** localisation algorithms have similar error values and standard deviations. However, their error distributions are very different and we can uncover further insight about localisation behavior by closely studying them. The distribution axial error of the latter has $\lambda/10$ peaks compared to the others' smooth distribution. That points towards jumps in the localisations. We hypothesize that this will cause a significant increase in the number of false negatives and a decrease in the number of true positives which can be verified in



[fig. 2.4a], $TP_{WA} = 180\text{ k}$, $TP_{(Cub-interp)} = 178\text{ k}$ and $FN_{WA} = 289\text{ k}$, $FN_{(Cub-Interp)} = 290\text{ k}$.

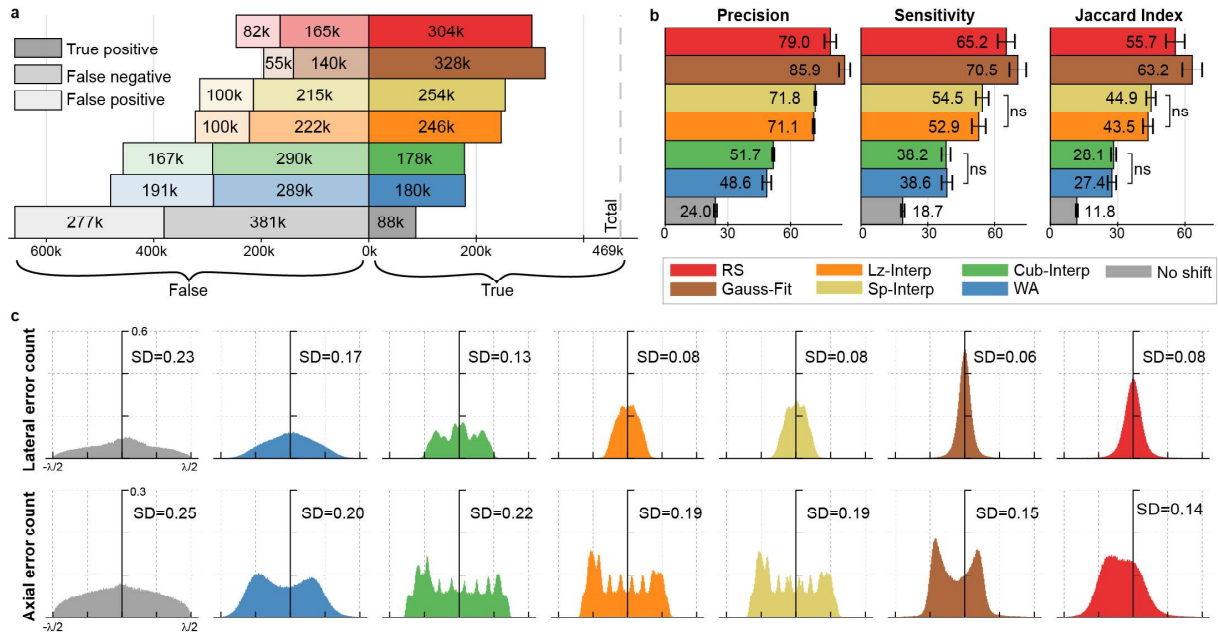


FIGURE 2.4 – Directional errors and statistical indices for performance on the dataset "in silico Flow" at 30 dB. **a**, Statistical measures of the different localisation schemes for dataset "in silico Flow". The left direction indicates the false ensemble, the right, the true ensemble. The total number of points simulated is 469 000. **b**, Statistical indices based on statistical measures for the different localisation schemes in percent. Means values of 20 blocks of 1000 continuous frames. Error bars represent $\pm s.d.$. Unpaired two-sample t-test of the means of the different algorithms always returns p-values lower than 5 % except when "ns" is specified (non-significant, $p>0.05$). **c**, Lateral and axial error distributions for the different localisation schemes. Some of these distributions have skew for example the spline and Lanczos interpolation schemes in the lateral direction. λ represents the wavelength. ($N>100\,000$)

The largest standard deviation of the lateral error was found for the no-shift method as expected. For the axial error, the algorithms have standard deviations between 0,06 and 0,23, with the lowest being the GF and the highest being the no shift. For the Gauss-Fit and RS-based algorithm, their lateral standard deviation error is around half lower than their axial error. The Lanczos and Spline interpolation schemes have similar ratios between the lateral and axial error standard deviation. The histogram distributions in the lateral direction for these algorithms seem to follow a Power-law with a high exponent whereas the weighted average, Lanczos, and spline kernel-based interpolation follow a linear law. The axial error distributions all present sharp peaks in different patterns. The most notable pattern is the fork pattern at $\lambda/10$ on the interpolation-based methods reproducing the interpolation grid used. Another pattern present in the radial symmetry and Gaussian fitting-based methods takes the shape of two sharp peaks on either side of the center value showing a bimodal behavior where the microbubble is localized in two preferred locations outside of the actual center. The RMSE is highly affected by this difference in localisation in both directions and while the RMSE of the radial symmetry and Gaussian fitting-based schemes are better than the others, the improvement in localisation



brought by these algorithms in the lateral direction is diminished in the final value of the RMSE. These errors were calculated for seven different SNR and are presented in Supplementary Figures 3-3.

The various algorithms spatially shift the expected localisation in different ways. To study this effect more precisely, it is useful to look at the results of the **PSF** simulation. The results are presented in [fig. 2.5]. The two main results are visible at once : first, the interpolation-based algorithms are scarcely affected by noise as they only take into account the closest neighboring sample to build the final function, and second, they exhibit a quite high standard deviation of their errors in the axial direction ($sd(err_{axspline}) = 0,19\lambda$, $sd(err_{axcubic}) = 0,22\lambda$). Putting it into perspective when plotting the absolute error at each of the $\lambda/21$ grid points helps to understand the dynamics of the noise impact [fig. 2.5b]. When the SNR diminishes, the errors of the best-ranked algorithms tend to show the bimodal behavior of the worst-ranked : axial and lateral errors are distributed in two bands in each direction up until a certain SNR value. At 15 dB the weighted average exhibits this behavior very clearly for the lateral error while the **GF** and **RS** have an almost uniform distribution. All distributions and maps are presented in Supplementary Figures 2-5 to 2-6 and 3-3. If we look more closely at the intensity profiles generated by our framework [fig. 2.5c], we can see that displacement in any direction induces a displacement of the maximum amplitude.



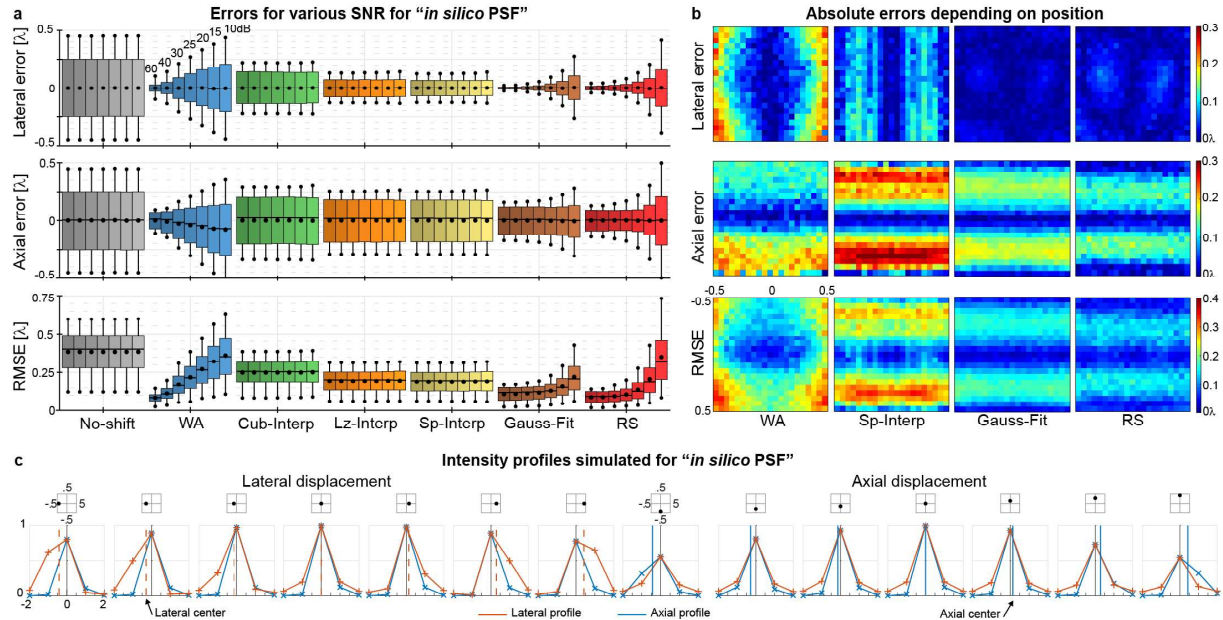
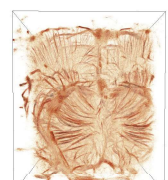


FIGURE 2.5 – Study of PSF non-uniformity in direction and its effect on localisation.

a, Lateral, axial and root mean square errors averages with standard deviations measured for the different localisation schemes on the dataset "in silico PSF" with different SNR. Errors are standard deviations. Bold center lines show medians, upper and lower box limits show the upper and lower quartiles, whiskers represent the first 5 % and 95 % quantiles. Round markers show mean values. ($N = 2646$) **b**, Absolute lateral, axial, and root mean square errors for each position where a scatterer was simulated inside the $\lambda \times \lambda$ grid with a SNR of 30 dB. λ represents the wavelength. ($N = 6$ per pixel) **c**, $5\lambda \times 5\lambda$ PSF simulated for a scatterer displaced in the $\lambda \times \lambda$ grid with $\lambda/7$ step. The intensity profiles demonstrate the inability of the wavelength-driven system to accurately reflect sub-wavelength displacement. The dashed lines represent the true position of the scatterer simulated.

However, even when moving close to the neighboring pixel situated ($\lambda/5$) further from the center, the maximum amplitude remains at the center of the pixel ($\{x, z\} = 0$). The maximum drop in intensity for each displacement is 12 dB below the peak amplitude on the connected components of the central pixel. This means that the bimodal behavior observed above in the axial error is due to low SNR that prevents the algorithms to use the information present in the neighboring pixels to perform accurate localisation. This confirms that the interpolation schemes don't vary with SNR as much as the other schemes as they only use 3 points to perform the interpolation. At SNR lower than 15 dB, localisation might fail in the **WA** and **RS** schemes at giving accurate enough results and providing enhanced resolution in the axial direction. The spatial frequency peak to baseline analysis detailed in the methods section 2.7 is presented in [fig. 2.7]. The cubic interpolation has a large score that is in line with what is described in the next section. The **Sp-Interp** and **WA** seem to have the same level of gridding. The radial and Gaussian fitting schemes come out on top with values almost 3 times less than the worst scheme.



2.3.4 Image quality metrics *in silico* and *in vivo*

With the provided datasets, both simulated and real microcirculation can be evaluated with the various algorithms. For instance, [fig. 2.6] shows the whole view of the ULM rendering of the simulated microcirculation. There are notable differences in how well algorithms manage to recover the initial shapes. In some cases, the overall contrast of the structures compared to the target is lower, with some vessels or part of vessels disappearing for example in the no-shift or cubic interpolation schemes. The horseshoe pattern and ULM watermark [fig. 2.6b] are the hardest structures to recover, few algorithms seem to perform well. Gauss-Fit/RS/Sp-Interp seem to yield the rendering closest to what was simulated, especially the curvature before and after the horseshoe. This shape is interesting as it is similar to saccular aneurysms. The smallest tubes are correctly represented in most cases but the separation index presented in [fig. 2.3] gives us an idea of the maximum resolution attainable which is the gold standard for resolution determination.

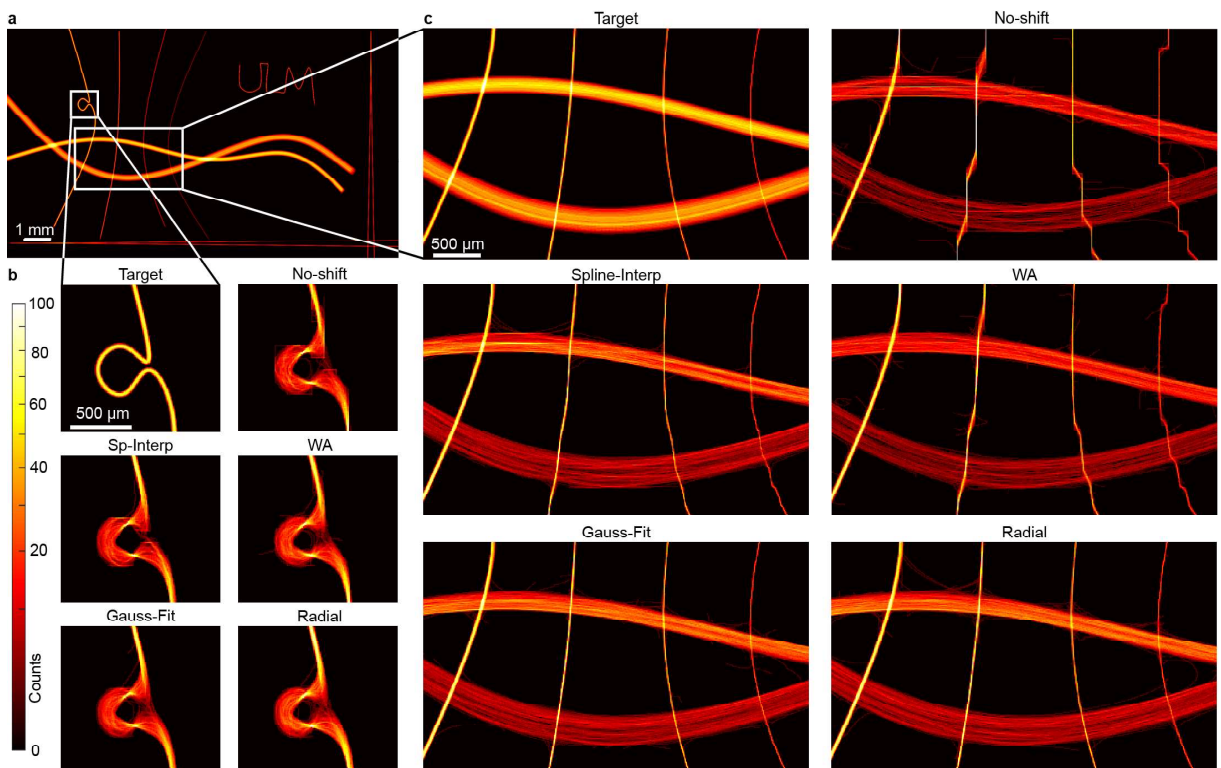


FIGURE 2.6 – 2D ULM density-based renderings of "in silico Flow" along with a focus on particular areas. The different renderings are obtained by giving each pixel in the image a value that is the number of trajectories passing through that coordinate. **a**, Target to be recovered by the algorithm. Composite rendering of 20 000 frames. **b**, Zoomed in renderings for the different localisation schemes on the horseshoe pattern. **c**, Zoomed in renderings for the different localisation schemes on structures with various diameters and characteristics.

The no-shift is valuable to study a hypothesis made in a previous paper about 3D ULM [37] stating that the grid effect appears because of erroneous localisation in areas of low SNR. Because the no-shift does not involve sub-pixel localisation, it should suffer the most from the grid effect



and one can see that it does, appearing in all of the structures smaller than the wavelength of the ultrasound sent ($100\text{ }\mu\text{m}$). Some behaviors are only visible when zooming in [fig. 2.6c]. The **WA** and the **Cub-Interp** scheme seem to suffer similar grid effects on the same tubes. The **Sp-Interp** only suffers gridding on the two smaller curved tubes (10 and $5\text{ }\mu\text{m}$). The **Gauss-Fit** and **RS**, on the other hand, adapt completely and do not suffer from any gridding on any curved tubes. More renderings are produced in Supplementary Figures 3-1, 3-2, 4-2, and 4-3. We devised an index to measure the grid-effect by a spatial frequency peak to baseline analysis in both directions. The value of that index grows with the severity of gridding. The values are reported in [fig. 2.7] next to the renderings of the brain vasculature. The no-shift-based ULM performs very poorly *in vivo* as predicted by the simulation and has the highest gridding index. The vessels in the cortex rendered by that scheme suffer from considerable gridding making their structure disorganized. The **Cub-Interp** also suffers from gridding as predicted, however, the **WA** localisation-based ULM is in appearance not gridded. To further investigate the effects of localisation, we zoomed in on a specific subcortical region where the grid effect is maximum, and where there is a large variety of vessel sizes [fig. 2.7b]. Our previous conclusion holds partially. The **Cub-Interp** is still massively subjected to gridding and we can see some gridding appearing in specific regions in **WA** (indicated by white triangles). For the four best-ranked algorithms, almost no gridding is present in the images *in vivo*. One considerable difference can be noted though between the **RS**-based ULM and the interpolation schemes : the vessels seem more detailed and sharper in the interpolation schemes. In **RS**, there seems to be a lot of small crossing trajectories in between the brightest and largest vessels.

Further insight can be drawn from [fig. 2.8] where the other *in vivo* datasets are presented. In the kidney, where the vasculature is organized differently than in the brain, these small crossing trajectories are not observed for the **RS** scheme. In the tumor, the vasculature is disorganized but no crossing trajectories are observed anyway. The difference between the best of the interpolation schemes (**Sp-Interp**) and the GF or **RS** algorithms is notable in the tumor where fewer vessels are being picked up by the former than the latter. The saturation curves, counting the number of illuminated pixels throughout the reconstruction, show us the capacity of algorithms to detect new structures. When interpolated based localisations saturate, **WA/Gauss-Fit/RS** are still recovering new pixels in the image. Finally, the **RS** obtain the highest final saturation value at 48,2 %, 1,9 % above the Weighted-Average.



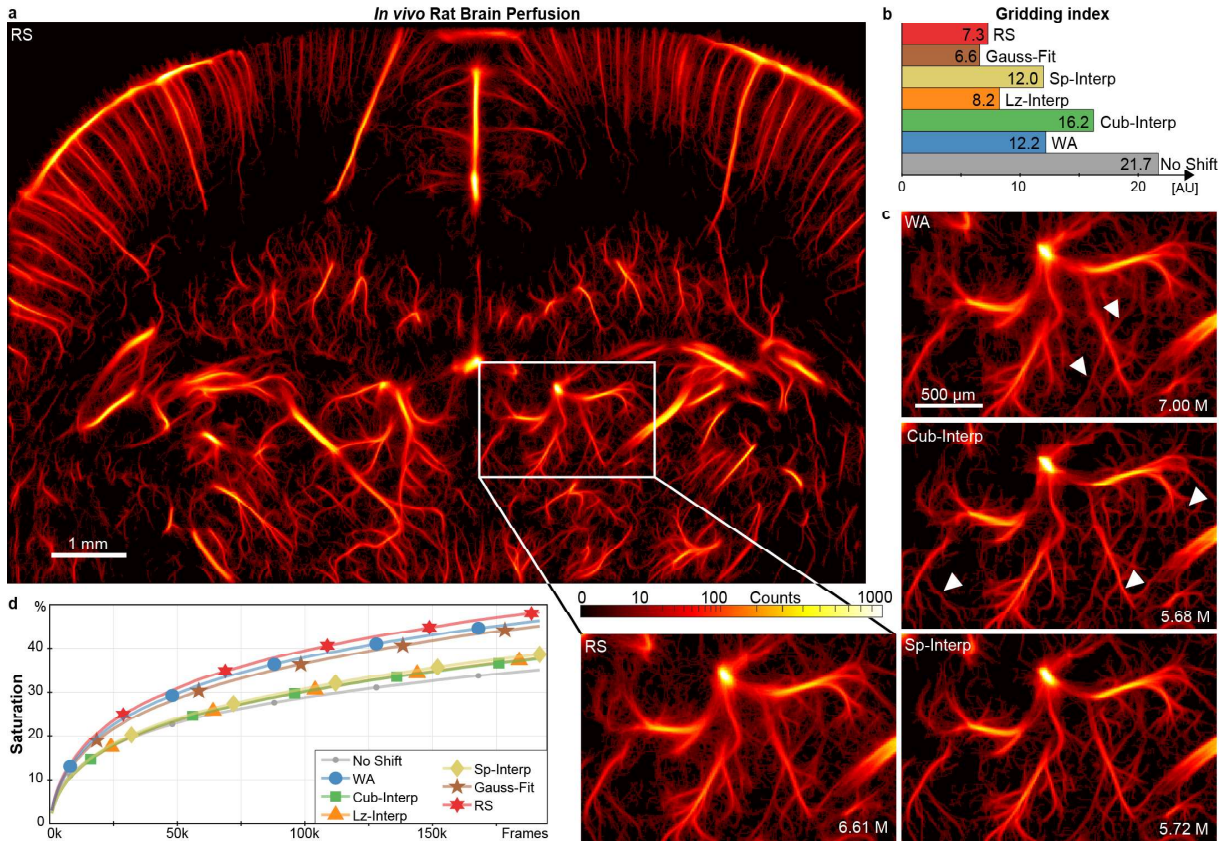


FIGURE 2.7 – 2D ULM density-based renderings of "in vivo" rat brain perfusion", with gridding index and saturation. The different renderings are obtained by giving each pixel in the image a value that is the number of trajectories passing through that coordinate. **a**, Rat brain rendering using radial localisation algorithm. Composite rendering of 192 000 frames. **b**, Gridding index calculated on the dataset "in vivo" rat brain perfusion" for every algorithm. **c**, Zoomed in portions of rat brain ULM using cubic interpolation, weighted average, spline interpolation, and radial symmetry-based localisations. **d**, Saturation coefficient calculated for each algorithm. For more detailed renderings, see Supplementary Figures 4-2 to 4-3

The results obtained on the three other *in vivo* datasets are presented in [fig. 2.8] (see also Supplementary Figures 4-5 to 4-7). The patterns described in the previous dataset still hold. In the *in vivo* rat brain bolus, the superiority of the GF and RS algorithms is confirmed, the overall score obtained by the RS is even higher than its score on the rat brain perfusion dataset. This superiority and the GF algorithms' high-quality imaging is best illustrated with the tumor where few vessels are present and are characterized by a disorganized structure. The GF and RS algorithm depict evidently more vessels than the other schemes. The gridding effect is clearly seen in the WA and Cub-Interp localisation schemes. As for the Sp-Interp, its imaging quality is quite high for example in the kidney, it is almost identical to the GF algorithm, but in the tumor dataset, we can see clear evidence that it localizes fewer vessels than GF and RS. The partial score (obtained from time, gridding, and saturation) difference between rat brain and tumor for the RS is 23 % while for the Weighted Average it is considerably less at 15 %. This difference for the interpolation-based schemes is interestingly constant at 22 %. For the no-shift, the ratio is 19 %.



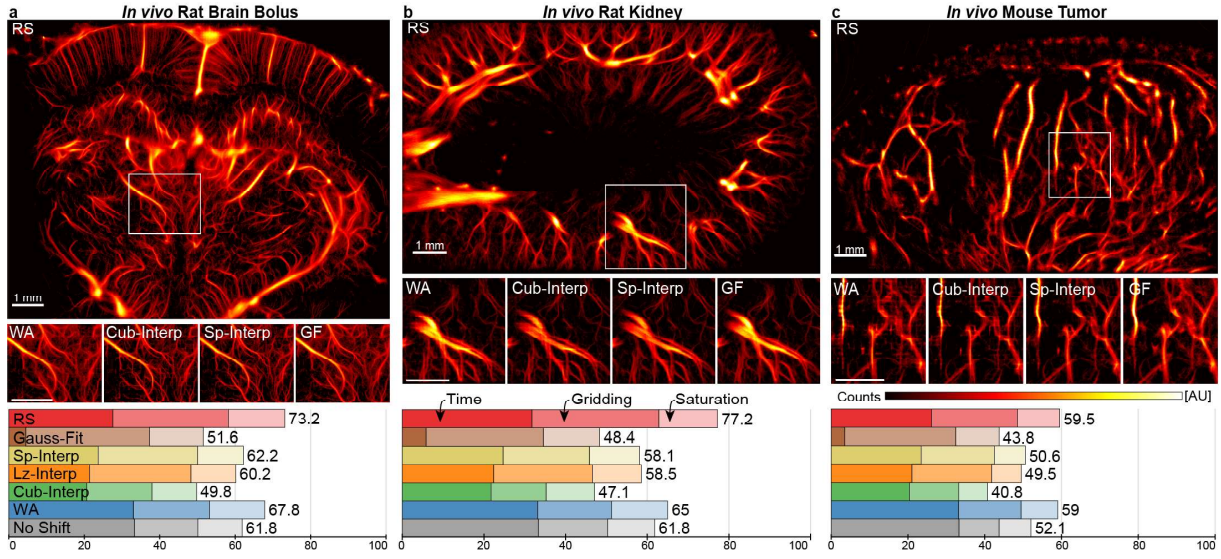


FIGURE 2.8 – 2D ULM density-based renderings of 3 other *in vivo* datasets, with partial scores. Density renderings obtained with radial symmetry are presented for 3 other *in vivo* datasets from the rat brain, rat kidney, and mouse tumor. Below each image is presented a cropped area (in white) of the same respective datasets obtained with Weighted Average, Cub-Interp, Sp-Interp, and Gaussian fitting renderings. Three dataset-specific metrics are presented on each of these datasets for all localisation algorithms, computation time, gridding index, and saturation index. **a**, *In vivo* rat brain imaging obtained by injecting microbubbles with bolus in the tail vein. The imaging plane acquired is different from the previous dataset presented. Noise is present on the far left corner of this dataset due to the remaining bone presence. Composite rendering of 170 000 frames. **b**, *In vivo* rat kidney imaging obtained after isolating the kidney outside of the abdomen. Motion has been corrected for. The vascular structure is clearly recognisable with the two main arteries and veins on the left of the image. Composite rendering of 188 000 frames. **c**, *In vivo* mouse tumor imaging obtained on a subcutaneous back tumor. The vascular structure here is clearly disorganized and not as sharp as in the kidney and brain images. Composite rendering of 30 000 frames. All scale bars, 1 mm.

2.4 Discussion

The ULM workflow evaluated here includes every step after data acquisition/generation to final rendering, along with the calculations of the various proposed metrics for ULM quality. The localisation step alone was benchmarked as it is the most variable aspect of ULM algorithms used by different teams. However, filtering, ultrasound acquisition parameters, contrast agent types, and tracking algorithms should also be studied. Partial studies have been made about filtering [37,38], contrast agent types [39,40] ; ultrasound acquisition parameters [22] as well as tracking algorithms [38] but it is hard to draw general conclusions for the techniques as these papers do not use the same datasets. We hope that with the datasets provided in this paper, comparison and accurate characterisation of all the steps will be feasible. Devising metrics to compare and rate specific aspects of localisation is a crucial step in providing a better understanding of super-resolution imaging. Visual scoring by radiologists, neurologists, or physiologists will be required to establish quality grading for each application. However, ULM will first need to gain better uniformity through quantitative and objective metrics assessments.



Thanks to the different datasets generated, we can quantify the influence of PSF inhomogeneity, size, complexity, the position of the shape to recover, and behavior *in vivo* of the localisation schemes. The *in vivo* datasets are particularly important as they validate the different approaches in a pre-clinical setting. Specifically, they focus on brain, kidney, subcutaneous tumors which have very different vascular organisations and exhibit different experimental characteristics. For example, the tumor and kidney images will be subjected to more significant breathing motion, the tumor will also be fed by disorganized and low perfused vessels. The metrics were chosen to be as universal as possible and should work in any workflow, especially the ground truth-based metrics. The availability of the *in vivo* datasets should be seen as an incentive to both enhancing existing localisation algorithms and comparing the imaging quality of new *in vivo* applications. These *in vivo* datasets can also be used to try new approaches without going through the many stumbling points strewn along with preclinical experimentation.

We think the metrics presented here could be used whenever a new processing step or technology for ULM is implemented. Firstly, the improvement in localisation following the integration of this innovation should be characterized by using the "*in silico*" PSF and "*in silico* Flow" datasets. Rather than relying on the full width at half maximum of vessels, these metrics are based on the ground truth and thus are more accurate in quantifying localisation improvements. Secondly, the increase in the number of localisations should be quantified by using the statistical indices (True Positive, False Negative, and Positive), and the impact of that increase be measured with the Separation Index thanks to the codes available on the platform. Finally, we recommend that the impact of any innovation in ultrasound super-resolution is benchmarked on *in vivo* data as this technique's main application is pre-clinical and clinical imaging of the microvasculature. In order to include this, the *in vivo* datasets given here should be used as databases and the metrics Number of detections, Saturation, Gridding Index, and Processing Times should be computed and discussed in the report. The combination of these scores in a global score (identical to the PALA global score or with different weights to reflect other scenarii) is made easy by the dynamic table on the platform and will allow the community to evaluate the innovation at a quick glance.

An interesting aspect brought by the distribution errors point of view is the peaks present in the cubic, Lanczos, and spline interpolation schemes for the axial error. They are periodic with a frequency corresponding to the $\lambda/10$ interpolation grid. This would lead to a clear pattern on the final images.

On image quality metrics, we notice that the grid effect is especially present for interpolation-based localisation algorithms. It is very similar to quantisation in its form and as the no-shift method confirms, it is due to errors in the localisation. This means that in interpolation schemes, gridding comes from a reprojection of the localized center towards the center of the original pixel grid. It can be linked to low SNR in certain regions following this line of thought : if SNR is low, the full width at half maximum of the intensity increases so much that covered by the clutter noise, not enough information is present in the profiles to perform an accurate interpolation or localisation. When confronted with low SNR images, the algorithms tend to calculate the super-resolved center very close to the original center because it lacks sufficient signal, and thus



all positions align along one line, tracing that gridding pattern. This is confirmed by looking at where gridding happens in **Lz-Interp** and **Sp-Interp** schemes *in silico* or *in vivo*. In the large vessels, the number of events is sufficient to compensate for that effect, but for smaller vessels, the density of microbubbles is too low. This can be seen in the tumor images.

As such, attention should be paid to the reconstruction grid used for rendering. Decreasing the pixel size too much would increase the grid effect and the interpolation kernels, making the calculations more time-consuming. *In vivo*, the interpolation factor depends on the maximum theoretical resolution attainable, and as such, we advise that the super-resolved image pixel size and the maximum theoretical resolution be matched. One can note that even though localisation is performed poorly in the no-shift scheme, the rendering still appears believable and that should be kept in mind when evaluating the quality of ULM. Additionally, as was seen in the no-shift localisation scheme, if the reconstruction grid is too fine but the tracking algorithm contains an interpolation of tracks or smoothing, the grid effect may disappear and some artifacts may appear. These artifacts will lead to erroneous velocity estimations which can be measured and characterized by looking at the Poiseuille distributed profiles for these small vessels. Another difference to be noted is the lower gridding index calculated for **WA** compared to **Sp-Interp** although in [fig. 2.7b] the gridding effect is clearly higher. With 7,00 M events localized in the *in vivo* rat brain perfusion dataset, **WA** is the algorithm that localizes the most events (1,3 M more than **Sp-Interp**). The lower precision and higher **RMSE** compared to the **Sp-Interp** means that the final rendering contains a lot more erroneous localisations thus decreasing the principal peaks' amplitude in the frequency analysis devised for the gridding index.

In vivo, interpolation-based localisations seem to have a very sharp delineation of the vessels whereas **RS/Gauss-Fit** have many small trajectories going in and out of the most intense vessels. This makes the image obtained by the spline interpolation localisation look better than that obtained with the radial symmetry-based localisation. The latter looks like it has more noise than its interpolation-based counterpart. However, the *in silico* metrics tell us that the **RS** localisation is more sensitive and precise, meaning that it localizes microbubbles more correctly. It is confirmed by looking at the total number of particles localized [fig. 2.4], where the increase in the number of microbubbles localized in the radial symmetry-based algorithm is 21 %, and by the saturation, 4 % higher than the second algorithm. We hypothesize that the small trajectories in between vessels are also small vessels that can represent the capillary bed. When looking at how the kidney and tumor images are depicted by the different algorithms, we note the absence of cross trajectories. The duration of ultrasound imaging in these organs does not allow to represent the capillary bed clearly as the recovery of small vessels needs longer acquisition times. If the cross trajectories were due to noise, however, we would see them regardless of recording duration. A possible way to verify this *in vivo* would be to have access to the ground truth for example by observing fluorescently labeled microbubbles with ULM and optical imaging. A recently published study has indeed used such microbubbles [41]. Although coming in second after the Gaussian fitting algorithm in precision, and Jaccard index, the radial symmetry remains a good candidate for analysis of the capillary bed. Globally if time and low **RMSE** are more critical than an accurate classification of microbubbles, then the radial symmetry should be favored.



The time factor, measured for the fastest algorithm, is critical to the fast testing of many different parameters. If the algorithm of localisation runs for hours before being able to deliver a full image, changing parameters and waiting for the result will take days. This becomes critical in 3D as the third dimension makes everything considerably more complex. In our team, we have chosen to give priority to speedy calculations. That meant that in 2D, it only takes us 3 minutes to perform full ULM on 192 000 images which is less than the total acquisition time (4 minutes). Our computer is largely above average in terms of performance (Intel Core i9 @ 2,9 GHz 12 cores, NVidia RTX 2080Ti, 128 GB RAM @ 2133 MHz) but the ratio of speed improvement would be similar for any machine. This implementation appears much faster than many other algorithms. It improves the applicability of ULM, by allowing a simultaneous acquisition and reconstruction. In a clinical setting, that also means that the practitioner does not have to wait for its result and can either make another image in a matter of minutes or deliver his diagnosis.

The PALA global score we have devised and presented here aims at compiling all of these different metrics to aid algorithm selection. Our own defined global score was aimed at favoring fast and low error algorithms. However, one might want to favor calculation time above all other metrics for real-time applications or 3D. To do this we provide a dynamic table in supplementary (**PALA_GlobalScores_DynamicTable.xlsx**) (see Supplementary figures 5-2 to 5-4) where 6 different scenarios were designed to reflect experimental requirements : Non-weighted, 3D ULM, 2D scanning, Real-time, Low SNR, and our own defined global score. An additional line called New Entry allows the reader to set its own set of weights.

Several limitations remain in this study. For instance, the localisation is performed on microbubbles imaged at a high-frequency (15 MHz), limiting the effects linked to the resonant oscillations of microbubbles [17]. While that allows all of the results on the errors to be readily transposable to other frequencies, this is only applicable if linear imaging is used. Also as we have no access to ground truth *in vivo* at these depths in living animals, the structure of the capillary can only be hypothesized. We have not included the impact of beamforming techniques aimed at enhancing the PSF and CNR, as well as the different tracking algorithms available for ULM. However, thanks to the versatility of our framework, these can be easily included and benchmarked ad hoc. This versatility can be put to use to develop new metrics. One very valuable metric would be an index to benchmark the quality of ULM algorithms in between organs and in between datasets coming from different groups. Comparing organs that have a very different vascular organisation, such as the kidney or the brain, remains a challenge. In 2D, the possibility to have an atlas of the vasculature of the rat's brain could be explored but will probably run into out-of-plane related issues (motion, size of the plane at focus, interrupted tracks, reprojection of vessels).

The noise simulated in the *in silico* dataset is a simple model aimed at imitating clutter noise. Added to the beamformed images, it does not take into account jitter, false peak errors in the radiofrequency data, readout noise from the electronics, nor does it represent potential motion. As the *in vivo* data we have presented have been filtered with a spatiotemporal clutter filter, our aim, by choosing this simplistic approach, was to reproduce SNR values and aspects seen in the *in vivo* cases. However, thanks to the versatility of our platform, any noise model



could be added to the *in silico* dataset easily.

We hope that these algorithms, datasets, and metrics will improve the comparisons and discussions among the growing ULM community and allow more users with less ultrasonic expertise to exploit these new methods. Besides potentially becoming a valuable clinical imaging modality, ULM opens a new window to observe the microcirculation in-depth and complements other laboratory imaging methods that lack either resolution or penetration.

2.5 Outlook

We have developed a platform to analyze and measure the performance of the most used localisation schemes in Ultrasound Localisation Microscopy. This led us to integrate these in an open-source algorithm, which is available in the supplementary information, to facilitate the dissemination of the technique for research groups around the world. Furthermore, we provide the data and scripts needed to benchmark future techniques or other aspects of the ULM process. Also, these algorithms can be readily used on emerging contrast agents such as acoustically activated nanodroplets, biogenic gas vesicles, or novel imaging applications such as 4D ultrasound or non-linear imaging. This open framework could benefit from further development such as non-linear behavior simulation or tracking improvement. Finally, we have presented two novel algorithms, one of which obtains the highest score according to the criteria proposed here. With the advent of new artificial intelligence-based super-resolution methods, the metrics devised will help to compare and characterize such methods. We see great potential in the collective use of these resources to improve our knowledge of ULM, increase its quality, and provide better and faster imaging for 3D developments.

Reporting summary.

Further information on research design is available in the Nature Research Reporting Summary linked to this article.

Data availability

The main data supporting the results in this study are available within the paper and its Supplementary Information. All data generated in this study, including source data and the data used to make the figures, are available from zenodo with the identifier <https://doi.org/10.5281/zenodo.4343435>

Code availability

All the codes used for data acquisition and for data analysis referenced in this resource are available on a GitHub repository, along with potential updates and can be downloaded at <https://github.com/AChavignon/PALA>.



2.6 References

- [1] Tanter, M. & Fink, M. Ultrafast imaging in biomedical ultrasound. *IEEE Trans. Ultrason. Ferroelectr. Freq. Control* 61, 102–119 (2014).
- [2] Macé, E. et al. Functional ultrasound imaging of the brain. *Nat. Methods* 8, 662–664 (2011).
- [3] Macé, E. et al. High sensitivity brain angiography using ultrafast Doppler. in (2010). doi :10.1109/ultsym.2010.5935810.
- [4] Demene, C. et al. Spatiotemporal Clutter Filtering of Ultrafast Ultrasound Data Highly Increases Doppler and fUltrasound Sensitivity. *IEEE Trans. Med. Imaging* 34, 2271–2285 (2015).
- [5] Frinking, P., Segers, T., Luan, Y. & Tranquart, F. Three Decades of Ultrasound Contrast Agents : A Review of the Past, Present and Future Improvements. *Ultrasound Med. Biol.* 46, 892–908 (2020).
- [6] Couture, O., Besson, B., Montaldo, G., Fink, M. & Tanter, M. Microbubble ultrasound super-localisation imaging (MUSLI). in 1285–1287 (IEEE, 2011). doi :10.1109/ULTSYM.2011.6293576.
- [7] Olivier Couture, Mickael Tanter & Mathias Fink. Patent 889 Cooperation Treaty (PCT) /FR2011/052810.
- [8] Couture, O., Hingot, V., Heiles, B., Muleki-Seya, P. & Tanter, M. Ultrasound Localisation Microscopy and Super-Resolution : A State of the Art. *IEEE Trans. Ultrason. Ferroelectr. Freq. Control* 65, 1304–1320 (2018).
- [9] Errico, C. et al. Ultrafast ultrasound localisation microscopy for deep super-resolution vascular imaging. *Nature* 527, 499–502 (2015).
- [10] Christensen-Jeffries, K., Browning, R. J., Tang, M.-X., Dunsby, C. & Eckersley, R. J. In Vivo Acoustic Super-Resolution and Super-Resolved Velocity Mapping Using Microbubbles. *IEEE Trans. Med. Imaging* 34, 433–440 (2015).
- [11] Heiles, B. Ultrafast Volumetric Ultrasound Localisation Microscopy in vivo. in (2018).
- [12] Viessmann, O. M., Eckersley, R. J., Christensen-Jeffries, K., Tang, M. X. & Dunsby, C. Acoustic super-resolution with ultrasound and microbubbles. *Phys. Med. Biol.* 58, 6447–6458 (2013).
- [13] Lin, F. et al. 3-D Ultrasound Localisation Microscopy for Identifying Microvascular Morphology Features of Tumor Angiogenesis at a Resolution Beyond the Diffraction Limit of Conventional Ultrasound. *Theranostics* 7, 196–204 (2017).
- [14] O'Reilly, M. A. & Hynynen, K. A super-resolution ultrasound method for brain vascular mapping : Super-resolution ultrasound method for brain vascular mapping. *Med. Phys.* 40, 110701 (2013).
- [15] Song, P. et al. Improved Super-Resolution Ultrasound Microvessel Imaging With Spatiotemporal Nonlocal Means Filtering and Bipartite Graph-Based Microbubble Tracking. *IEEE Trans. Ultrason. Ferroelectr. Freq. Control* 65, 149–167 (2018).
- [16] Brown, J. et al. Investigation of Microbubble Detection Methods for Super-Resolution Imaging of Microvasculature. *IEEE Trans. Ultrason. Ferroelectr. Freq. Control* 66, 676–691 (2019).
- [17] Christensen-Jeffries, K. et al. Microbubble Axial Localisation Errors in Ultrasound Super-Resolution Imaging. *IEEE Trans. Ultrason. Ferroelectr. Freq. Control* 64, 1644–1654 (2017).
- [18] Kanoulas, E. et al. Super-Resolution Contrast-Enhanced Ultrasound Methodology for the Identification of In Vivo Vascular Dynamics in 2D : Invest. Radiol. 54, 500–516 (2019).
- [19] Ackermann, D. & Schmitz, G. Detection and Tracking of Multiple Microbubbles in Ultrasound B-Mode Images. *IEEE Trans. Ultrason. Ferroelectr. Freq. Control* 63, 72–82 (2016).
- [20] Luke, G. P., Hannah, A. S. & Emelianov, S. Y. Super-Resolution Ultrasound Imaging in Vivo with Transient Laser-Activated Nanodroplets. *Nano Lett.* 16, 2556–2559 (2016).
- [21] O'Reilly, M. A. & Hynynen, K. A super-resolution ultrasound method for brain vascular mapping : Super-resolution ultrasound method for brain vascular mapping. *Med. Phys.* 40, 110701 (2013).
- [22] Song, P., Manduca, A., Trzasko, J. D., Daigle, R. E. & Chen, S. On the Effects of Spatial Sampling Quantisation in Super-Resolution Ultrasound Microvessel Imaging. *IEEE Trans. Ultrason. Ferroelectr. Freq. Control* 65, 2264–2276 (2018).
- [23] Hansen, K. B. et al. Robust microbubble tracking for super resolution imaging in ultrasound. in 2016 IEEE International Ultrasonics Symposium (IUS) 1–4 (IEEE, 2016). doi :10.1109/ULTSYM.2016.7728793. [24] Heiles, B. et al. Ultrafast 3D Ultrasound Localisation Microscopy using a 32x32 Matrix Array. *IEEE Trans. Med. Imaging* 13 (2019).
- [25] Soulioti, D. E., Espíndola, D., Dayton, P. A. & Pinton, G. Super resolution imaging through the human skull. *ArXiv181110653 Cond-Mat Physicsphysics* (2018).
- [26] Viessmann, O. M., Eckersley, R. J., Christensen-Jeffries, K., Tang, M. X. & Dunsby, C. Acoustic super-resolution with ultrasound and microbubbles. *Phys. Med. Biol.* 58, 6447–6458 (2013).



- [27] Zhang, G. et al. Acoustic wave sparsely activated localisation microscopy (AWSALM) : Super-resolution ultrasound imaging using acoustic activation and deactivation of nanodroplets. *Appl. Phys. Lett.* 113, 014101 (2018).
- [28] Zhu, J. et al. 3D Super-Resolution US Imaging of Rabbit Lymph Node Vasculature in Vivo by Using Microbubbles. *Radiology* 291, 642–650 (2019).
- [29] Huang, C. et al. Short Acquisition Time Super-Resolution Ultrasound Microvessel Imaging via Microbubble Separation. *Sci. Rep.* 10, 6007 (2020).
- [30] Parthasarathy, R. Rapid, accurate particle tracking by calculation of radial symmetry centers. *Nat. Methods* 9, 724–726 (2012).
- [31] Christensen-Jeffries, K. et al. 3-D In Vitro Acoustic Super-Resolution and Super-Resolved Velocity Mapping Using Microbubbles. *IEEE Trans. Ultrason. Ferroelectr. Freq. Control* 64, 1478–1486 (2017).
- [32] Desailly, Y., Couture, O., Fink, M. & Tanter, M. Sono-activated ultrasound localisation microscopy. *Appl. Phys. Lett.* 103, 174107 (2013).
- [33] Desailly, Y., Pierre, J., Couture, O. & Tanter, M. Resolution limits of ultrafast ultrasound localisation microscopy. *Phys. Med. Biol.* 60, 8723–8740 (2015).
- [34] Song, P., Manduca, A., Trzasko, J. D., Daigle, R. E. & Chen, S. On the Effects of Spatial Sampling Quantisation in Super-Resolution Ultrasound Microvessel Imaging. *IEEE Trans. Ultrason. Ferroelectr. Freq. Control* 65, 2264–2276 (2018).
- [35] Hingot, V. et al. Microvascular flow dictates the compromise between spatial resolution and acquisition time in Ultrasound Localisation Microscopy. *Sci. Rep.* 9, (2019).
- [36] Kuhn, H. W. The Hungarian method for the assignment problem. *Nav. Res. Logist. Q.* 2, 83–97 (1955).
- [37] Heiles, B. et al. Ultrafast 3D Ultrasound Localisation Microscopy using a 32x32 Matrix Array. *Accept. IEEE Trans. Med. Imaging* 13 (2019).
- [38] Song, P. et al. Improved Super-Resolution Ultrasound Microvessel Imaging With Spatiotemporal Nonlocal Means Filtering and Bipartite Graph-Based Microbubble Tracking. *IEEE Trans. Ultrason. Ferroelectr. Freq. Control* 65, 149–167 (2018).
- [39] Luke, G. P., Hannah, A. S. & Emelianov, S. Y. Super-Resolution Ultrasound Imaging in Vivo with Transient Laser-Activated Nanodroplets. *Nano Lett.* 16, 2556–2559 (2016).
- [40] Zhang, G. et al. Acoustic wave sparsely activated localisation microscopy (AWSALM) : Super-resolution ultrasound imaging using acoustic activation and deactivation of nanodroplets. *Appl. Phys. Lett.* 113, 014101 (2018).
- [41] Lowerison, M. R., Huang, C., Lucien, F., Chen, S. & Song, P. Ultrasound localisation microscopy of renal tumor xenografts in chicken embryo is correlated to hypoxia. *Sci. Rep.* 10, 2478 (2020).
- [42] Forsberg, F., Leeman, S. & Jensen, J. A. Assessment of hybrid speckle reduction algorithms. *Phys. Med. Biol.* 36, 1539–1549 (1991).
- [43] Ledoux, L. A. F., Brands, P. J. & Hoeks, A. P. G. Reduction of the Clutter Component in Doppler Ultrasound Signals Based on Singular Value Decomposition : A Simulation Study. *Ultrason. Imaging* 19, 1–18 (1997).
- [44] Desailly, Y. et al. Contrast enhanced ultrasound by real-time spatiotemporal filtering of ultrafast images. *Phys. Med. Biol.* 62, 31–42 (2017).

Acknowledgements

The project has been funded by the European Research Council under the European Union Horizon H2020 program/ERC Consolidator grant agreement No 772786-ResolveStroke. The project was also supported by Agence Nationale de la Recherche (ANR), within the project ANR Predic and the Plan Cancer UICT. We thank the laboratories Institut Langevin and PhysMed Paris for technical support and particularly Line Rahal for helping with data acquisition. We thank Cyrille Orset (INSERM UMR-S U1237, Physiopathology and Imaging of Neurological Disorders, GIP Cyceron, Institut Blood and Brain @ Caen-Normandie (BB@C), Caen, France) for animals' preparation and perfusion of contrast agent and the biomedical imaging platform CYCERON (UMS 3408 Unicaen/CNRS, Caen, France), particularly, Hanadi Skeif and Vincent



Beaudouin for the micro-CT of brains. We would like to thank Ruslan Hlushchuk for all his valuable advices for μ Angiofil perfusion, David Maresca for useful discussion and our collaborators Franck Lager, Gilles Renault and Alba Nicolas-Boluda for helping with the mouse tumor model and the *in vivo* experiments.

Author contributions

All authors conceived the project. ET and PL are the main collaborators on the kidney and tumor experiments. BH and VH laid out the general framework and algorithm for ULM with contributions from all authors. BH wrote the original codes for localisation algorithms with significant improvements brought by AC. AC wrote the simulation framework and implemented the metrics. VH, AC, ET, and PL acquired *in vivo* data. BH wrote the manuscript with input from all authors. OC has directed the work of BH, AC, and VH as thesis/postdoctoral supervisor.

Competing interests

Baptiste Heiles, Arthur Chavignon, Vincent Hingot, Pauline Lopez and Elliott Teston declare no competing financial interests. Olivier Couture is a co-inventor of an ultrasound super-resolution patent (PCT)/FR2011/052810.

Additional information

Animal experimentation All animals received humane care in compliance European Community Council Directive of 22nd September 2010 (010/63/UE) and approved by the institutional committee C2EA-59 : "Comité d'éthique en matière d'expérimentation animale Paris Centre et Sud" under the protocol APAFIS #13363-2018020321116321 (rat brain), APAFIS #16874-2017122914243628 (rat kidney), the institutional committee C2EA-034 : "Comité d'éthique en matière d'expérimentation animale Paris Descartes", APAFIS #25169-202008071746473 (mouse tumor), and the institutional committee C2EA-54 "Comité d'éthique Normandie en matière d'expérimentation animale" under the protocol APAFIS #22544-2019093017523797 (rat brain with micro-CT)

2.7 Methods

2.7.1 Point Spread Function dataset ("*in silico* PSF")

The Point-Spread Function (PSF) simulation is designed to study non-uniformity effects on localisation and spatial sampling effect on the beamforming process. A point-like scatterer is simulated using the Verasonics Research Ultrasound Simulator (Verasonics Inc., Kirkland Washington, USA). The position of the scatterer is moved by $\lambda/7$ increments in both directions in a $\lambda \times \lambda$ space. For each of these positions, the radiofrequency response, as well as its beamformed image, was produced using 3 tilted plane waves emitted from a 15 MHz linear probe, with 128 elements spaced by one wavelength. The speed of sound was set to 1540 m/s.



2.7.2 *In silico* angiography dataset ("*in silico* Flow")

The media simulated comprised of 11 tubes with various geometries with various complexity (see [fig. 2.6] and Supplementary table 6-2, Supplementary Figure 2-1) :

Structure	Diameters	Maximal velocities
A pseudo double helix	3λ	$v_{max} = 3\lambda/\text{frame}$
	2λ	$v_{max} = 2\lambda/\text{frame}$
A curved tube with a constant diameter and a horseshoe pattern	$0,5\lambda$	$v_{max} = 0,5\lambda/\text{frame}$
3 curved tubes with 3 different diameters	$0,2\lambda$	$v_{max} = 0,2\lambda/\text{frame}$
	$0,1\lambda$	$v_{max} = 0,1\lambda/\text{frame}$
	$0,05\lambda$	$v_{max} = 0,05\lambda/\text{frame}$
4 spreading tubes with a constant diameter	$0,1\lambda$	$v_{max} = 0,9\lambda/\text{frame}$
A watermark comprised of the word ULM that does not serve other purposes but identification	$0,1\lambda$	$v_{max} = 0,4\lambda/\text{frame}$

To simulate moving microbubbles, we chose initial random positions in the tubes and recorded them as point-like scatterers. For each of these positions, a trajectory calculated by Poiseuille's law was assigned based on their position in the cross-section of the tube. We considered that microbubbles could not jump from one trajectory to another and so had to follow the same trajectory for as long as it is simulated. Using the Verasonics Research Ultrasound Simulator, we simulated radiofrequency and beamformed images of a moving scatterer in a $7 \times 14,9 \text{ mm}^2$ area insonified with 3 tilted plane waves with a 15 MHz linear probe, with 128 elements spaced by one wavelength. The simulation sequence was based on the Vantage example script (Vantage release 4.0.0) FlashAngles and adapted to save either radiofrequency data and beamformed images with $\lambda \times \lambda$ pixel size. The speed of sound was set to 1540 m/s. For each image in the two *in silico* datasets, we added clutter noise modeled by a Gaussian filtered white Gaussian noise (see Supplementary Figure 4-2). The parameters for the white Gaussian Noise were matched with a typical 30 dB noise present in our *in vivo* images : we used *wgn* MATLAB (The MathWorks, Inc., Natick Massachusetts, USA) function to generate a 0,2 ohm impedance noise, with a ± 10 dB amplitude. The resulting noise was then filtered using a 2D Gaussian kernel of size 0,7 pixel. Finally, the noise was added to the beamformed image by choosing an amplitude in dB between the maximum intensity value of the beamformed image and the average intensity of the generated noise. This process results in noised images, with a user-selected SNR, and a pseudo clutter with 20 dB of amplitude.

2.7.3 *In vivo* dataset ("*in vivo* rat brain perfusion" and "*in vivo* rat brain bolus")

All animals received humane care in compliance European Community Council Directive of 22nd September 2010 (010/63/UE) and approved by the institutional committee C2EA-59 : "Comité d'Ethique en matière d'Expérimentation Animale Paris Centre et Sud" under the protocol 2015-23. 8-10 weeks Sprague-Dawley rats were obtained from Janvier Labs (Le Genest-Saint-



Isle, France). The animals were kept for at least a week before surgery. Water and a commercial pelleted diet SAFE A04-10 (Augy, France) were available ad libitum. SAFE FLAKE sawdust was used as bedding, enrichment such as pieces of cardboard, paper tunnels were provided. After 5 minutes in the induction cage filled with a mix of air and 5 % of Isoflurane, the animal was placed on the back on a heated plate with a respiratory mask. The mix was replaced with O_2 mixed with 4 % of Isoflurane. The depth of the anesthesia was tested by the absence of withdrawal reflex when pinching the toes of the hind limb. A jugular vein catheter was then placed and craniotomy surgery was used to remove the skull on a window in between the Lambda and Bregma planes and 14 mm wide. 400 μ l of Sonovue microbubbles (Bracco Imaging®, Milan, Italy) were injected at a steady rate of 80 μ l/min to keep a stable concentration in the bloodstream or with boli in the second dataset. A continuous ultrasound acquisition comprised of 240 blocs (or 213 blocs for bolus dataset) of 800 frames taken at a compounded frame rate of 1000 Hz with 3 tilted plane waves [-3 ; 0 ; 3]° or ([-5 ; 0 ; 5]° for bolus dataset) using a 15 MHz centered frequency probe manufactured by Vermon®, Tours, France with a 0,1 mm pitch. Acquisitions lasted 4 min for the perfusion dataset, and 3 min 30 sec for the bolus dataset. Elevation focusing is provided through a plastic lens to reach 500 μ m at 8 mm. The radiofrequency data were beamformed on the ultrasound machine's GPU (SuperSonic Imagine, Aix-en-Provence, France) and transferred to an external hard drive for later processing. The microbubbles' SNR was measured on a filtered image as the intensity ratio between the 10 brightest microbubbles and the average image intensity.

2.7.4 In vivo dataset ("in vivo rat kidney")

All animals received humane care in compliance European Community Council Directive of 22nd September 2010 (010/63/UE) and approved by the institutional committee C2EA-59 : "Comité d'Ethique en matière d'Expérimentation Animale Paris Centre et Sud" under the protocol APAFIS #16874-2017122914243628. The same housing protocol and strain of rat were used as the animals used for the brain experiments. The kidney was exposed through a lumbotomy incision and placed on an acoustically absorbing material to facilitate imaging. A heat lamp was used to prevent hypothermia of the animal. Ultrasound gel was applied on top of the imaging area to provide coupling, Sonovue microbubbles (Bracco Imaging®, Milan, Italy) were injected in boli via a jugular vein catheter. A continuous ultrasound acquisition comprised of 240 blocs of 800 frames taken at a compounded frame rate of 1000 Hz with 5 tilted plane waves [-10 ; -5 ; 0 ; 5 ; 10]° using a 15 MHz centered frequency probe manufactured by Vermon, Tours, France with a 0,1 mm pitch. The acquisition lasted 4 minutes. Elevation focusing is provided through a plastic lens to reach 500 μ m at 8 mm.

2.7.5 In vivo dataset ("in vivo mouse tumor")

All animals received humane care in compliance European Community Council Directive of 22nd September 2010 (010/63/UE) and approved by the institutional committee C2EA-34 : "Comité d'Ethique en matière d'Expérimentation Animale Paris Descartes" under the protocol

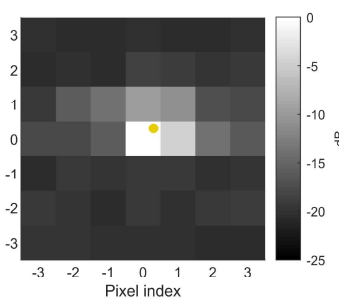


APAFIS #25169-202008071746473. For this study, MMTV-PyMT transgenic mice were back-crossed with FvB/NCrl mice (Charles River Laboratories, Wilmington Massachusetts, USA). A transplanted model of the MMTV-PyMT was used for this study. Tumor implantation was performed using primary tumors developed in donor mice. Donor mice with primary tumors of $\sim 10\text{--}15$ mm were killed and tumors were pooled, dissociated, and then re-injected orthotopically in receiver mice. Tumors were dissociated mechanically and incubated for 30 minutes at 37°C with DNase I (100 $\mu\text{g}/\text{ml}$, Roche Diagnostics GmbH, Mannheim, Germany), collagenase (1 mg/ml, Roche Diagnostics GmbH, Mannheim, Germany), and hyaluronidase (1 $\mu\text{g}/\text{ml}$, Sigma-Aldrich, St. Louis Missouri, USA) in RPMI with 2 % serum. After red blood cell lysis and filtration on a 70 μm sieve, the cell suspension was rinsed 3 times in PBS and used for tumor transplantation. Thus, 106 cells isolated from tumors of MMTV-PyMT mice were injected in 100 μl of PBS in the mammary fat pad of 8 weeks-old FvB mice. About 10 days after inoculation, transplanted PyMT tumors reached a diameter of ~ 6 mm. A continuous ultrasound acquisition comprised of 150 blocs of 200 frames taken at a compounded frame rate of 500 Hz with 5 tilted plane waves [-10 ; -5 ; 0 ; 5 ; 10] $^\circ$ using a 15 MHz centered frequency probe manufactured by Vermon, Tours, France with a 0,1 mm pitch. The acquisition lasted 2 min 30 sec. Elevation focusing is provided through a plastic lens to reach 500 μm at 8 mm.

2.7.6 ULM workflow and detection

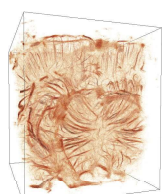
ULM is a multi-step method. The general layout is presented in [fig. 2.2] and Supplementary Figure 4-8. Firstly, one needs to acquire a large number of frames in the region of imaging. Then, a detection process takes place to enhance the signal of microbubbles. Close microbubbles are isolated. *In silico*, such a step is dispensed with as the signal-to-noise ratio is set high enough in the simulation. For the *in vivo* dataset, we use the Singular Value Decomposition approach [4,42,43]. By rearranging a continuous set of beamformed images as a Casorati matrix ($N_z \times N_x, N_t$), we will use the new basis given by the SVD to filter the tissue from the microbubbles according to its spatiotemporal decorrelation [44]. We remove the four highest energy vectors out of a basis of 800.

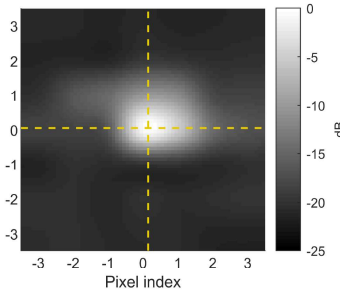
2.7.7 Localization algorithms



Simulated beamformed image centered on a microbubble. The pixel size is $\lambda \times \lambda$. The real position of the simulated scatterer is $20,3\lambda$ the lateral position, and $61,3\lambda$ the axial position and is represented by the yellow solid dot. To apply the localisation kernel, the full image is cropped and centered on the pixel with the highest intensity. The localisation kernel returns the position shift of the estimated. The No-shift algorithm will always return a null shift.

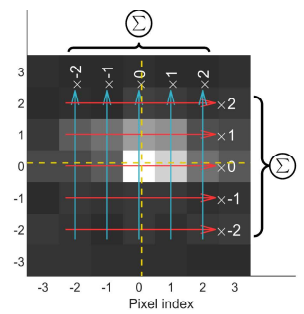
The image is rendered with a log compression.





Interpolation based algorithm

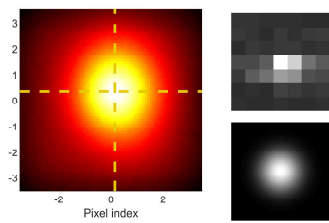
Simulated beamformed image centered on a microbubble with interpolation to illustrate interpolation-based algorithms. Each pixel is divided into 10×10 subpixels. Different localisation methods can be used : cubic, Lanczos, spline.



Weighted average algorithm

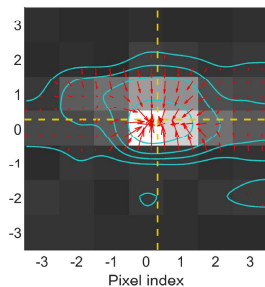
Simulated beamformed image centered on a microbubble. Arrows illustrate the process of weighted average algorithm. For the axial shift, the image intensity (without log compression) is summed over the 5 lateral pixels, and weighted with $[-2;-1;0;1;2]$ coefficients and divided by the total intensity.

$$z_{shift} = \frac{\sum_{i=-2}^2 \sum_{j=-2}^2 I(i,j) \cdot j}{\sum_{i=-2}^2 \sum_{j=-2}^2 I(i,j)}$$



Gaussian fitting algorithm

The top right-hand image is the input image of a centered microbubble with a log compression. The bottom right-hand image shows the Gaussian function used for the fitting.



Radial symmetry algorithm

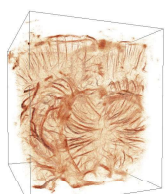
Simulated beamformed image centered on a microbubble with equipotential lines plotted in blue. The red arrows show the direction and amplitude of the gradient and point on the microbubble position.

2.7.8 Tracking algorithm

After microbubbles' positions are measured and stored, a tracking algorithm was implemented based on the Hungarian method or Kuhn-Munkres algorithm for assignment. For each particle, the squared distance to all of the particles in the subsequent frame is computed. We obtain a vector containing $N_{particles}$ ($t + dt$), the number of particles in the frame ($t + dt$). By applying the Kuhn-Munkres algorithm, we are able to find the optimal pairing for the subsequent frames by minimizing the total squared distance. We can calculate the velocities of each microbubble by differentiating each position in a trajectory according to the time vector.

2.7.9 Reconstruction

We build the final image by accumulating all the super-resolved positions of the microbubbles through time in a user defined pixel grid in a Maximum Intensity Projection fashion. The pixel



intensity represents the number of tracks passing through this pixel (see Supplementary Figure 4-9).

2.7.10 *In silico* metrics

Thanks to the simulation tool, we have access to the ground truth and can devise numerical and several statistical metrics based on classification :

- the error of localisation in two directions Z, X and calculate the average root mean square error (**RMSE**). $(z^0; x^0)$ represent the absolute position of the scatterer, and $(z; x)$ the position measured by algorithms.

$$\delta_z(i) = z_i^0 - z_i \quad \delta_x(i) = x_i^0 - x_i$$

$$RMSE = \frac{1}{N} \sum_i^n \sqrt{(x_i - x_i^0)^2 + (z_i - z_i^0)^2}$$

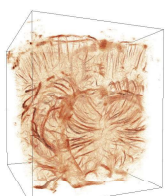
- True-positives (TP) : a microbubble was simulated and a microbubble was localized in a $\lambda/4$ excluding neighborhood
- False-positive (FP) : a microbubble was localized but no microbubble was simulated in the neighborhood
- False-negative (FN) : no microbubble was localized within a distance $\lambda/4$ of the simulated microbubbles
- the Jaccard index as : $JAC = TP/(FN + TP + FP)$
- positive predictive value (precision) p and recall (sensitivity) : $p = TP/(FP + TP)$, and $r = TP/(FN + TP)$
- separation index : minimal distance between inside borders of simulated canals, maximum resolution criteria

2.7.11 *In vivo* metrics

A visual analysis of the *in vivo* ULM rendering is done for each of the algorithms following several criteria : the number of localisations, likeliness of the trajectories, histogram of trajectory lengths, and visual aspects such as aliasing and branching vessels. The saturation curve represents the fraction of non-zero pixels in the image. The power spectral density of the spectral content in the (Z, X) directions of the intensity was calculated as :

$$F_z = FFT \left(\sum_x I(z, x) \right) \quad F_x = FFT \left(\sum_z I(z, x) \right)$$

The peak to the baseline value of the two first peaks of the power spectral density are summed in a logarithmic scale to quantify the amount of aliasing present in the image. For more details see Supplementary Figure 3-16. Finally, the computation time was evaluated for each algorithm



in the *in vivo* case and compared to the fastest algorithm. All 11 metrics can be summarized in a table (see Supplementary table 6-3).

Number	Measurement	Dataset		
		<i>In silico</i> PSF	<i>In silico</i> Flow	<i>In vivo</i>
1	Lateral error	X	X	
2	Axial error	X	X	
3	RMSE	X	X	
4	True Positive		X	
5	False Negative		X	
6	False Positive		X	
7	Gap		X	
8	Number of detections			X
9	Saturation			X
10	Gridding Index			X
11	Processing time			X

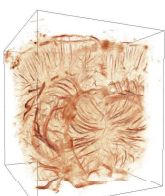
2.7.12 Conversion metrics to scores

Before building the global score, metrics are normalized into a percentage value. The table Supplementary table 6-4 explains the conversion from metrics results to scores. The global score is a weighted average of these individual scores.

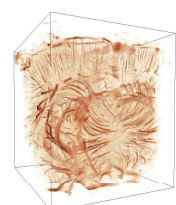
Metric	Unit	Conversion	Score Range
RMSE	Wavelengths	$Score(x_i) = 100 \cdot (1 - \frac{x_i}{0,5\lambda})$	$0\lambda : 100/100$ $0,5\lambda : 0/100$
Processing Time	Seconds	$Score(x_i) = 100 \cdot \left(1 - 0,5 \log_{10} \left(\frac{x_i}{min(x)}\right)\right)$	$min(x) : 100/100$ $100 \cdot min(x) : 100/100$
Separation Index	Wavelengths	$Score(x_i) = 100 \cdot (1 - \frac{x_i}{1\lambda})$	$0\lambda : 100/100$ $1\lambda : 0/100$
Gridding Index	dB	$Score(x_i) = 100 \cdot (1 - \frac{x_i}{30})$	$0 \text{ dB} : 100/100$ $30 \text{ dB} : 0/100$
Jaccard	%	$Score(x_i) = x_i$	$100 \% : 100/100$ $0 \% : 0/100$
Precision	%	$Score(x_i) = x_i$	$100 \% : 100/100$ $0 \% : 0/100$
Saturation	[%]	$Score(x_i) = x_i$	$100 \% : 100/100$ $0 \% : 0/100$

2.7.13 Micro angiography Computed Tomography (microangio-CT) with μ Angiofil

The animal was heparinized and carotid arteries were cannulated. The brain was perfused with saline (NaCl) at the animal's temperature to wash out the blood. Then the μ Angiofil (Fumedica AG, Switzerland) was perfused until the brain, tongue, and eyes became blue. After polymerisation of the μ Angiofil (at least 30 minutes), the head was removed and fixed with paraformaldehyde (PFA). Later, the brain was carefully extracted from the skull. The brain was



scanned with a pre-clinical micro-CT Siemens Inveon PET-CT (Siemens, Germany) with a voxel size of $37\text{ }\mu\text{m}$.



3 Annexes

3.1 Imagerie multimodale de la microvascularisation du cerveau : ultrasons et microtomographie aux rayons X

3.1.1 Problématique

La plupart des techniques d'imagerie *in vivo* ne permettent pas d'imager la microvascularisation en profondeur avec une résolution et une sensibilité suffisantes pour les artéries et veinules [fig. 1.14]. L'imagerie *ex vivo* par microtomographie aux rayons X [2.3.4] utilise un agent de contraste radio-opaque pour améliorer la sensibilité et le contraste, en utilisant des scanners dédiés haute résolution et des très temps d'acquisitions étendus (plusieurs heures).

La littérature actuelle ne présente pas de validation des capacités de l'**ULM** sur des organes complexes. Pour confronter l'imagerie **ULM** avec une autre technique de référence, le cerveau de rat a d'abord été imager par ultrasons avec retrait de l'os pariétal, puis perfusé avec un agent de contraste radio-opaque. Pour avoir une imagerie de tous les vaisseaux en **micro-CT**, l'intégralité du réseau vasculaire doit être rempli d'agent de contraste. La difficulté de cette perfusion est d'éviter la coagulation du sang dans le cerveau, et la présence de bulles d'air qui pourraient bloquer le passage du produit opaque.

3.1.2 Protocole pour le cerveau de rat

Le protocole de perfusion est détaillé dans la publication [Hlushchuk, 2020]. La méthode a été adaptée pour le cerveau de rat avec Cyrille Orset et les conseils experts de Ruslan Hlushchuk.

Suite à l'imagerie ultrasonore, l'animal est maintenu à une température de 38 °C et une injection d'héparine est effectuée pour prévenir la coagulation en vue du remplacement de tout le sang du cerveau par l'agent de contraste.

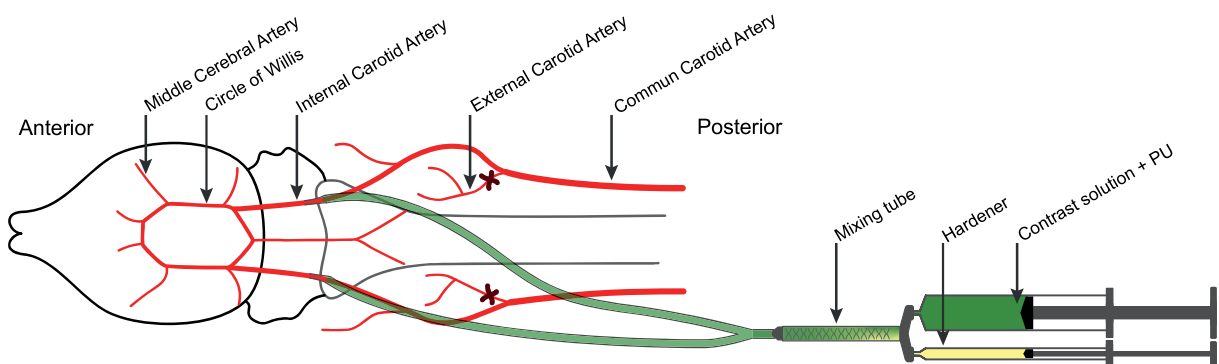
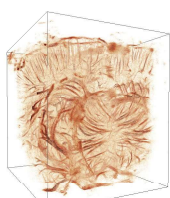


FIGURE 2.9 – Schéma de la perfusion de μ Angiofil (Fumedica) pour la microtomographie du cerveau de rat.

Deux cathéters sont nécessaires pour une perfusion optimale du cerveau, dans chaque artère carotide commune [fig. 2.9]. Les artères cérébrales externes sont ligaturées pour réduire le volume à perfuser et éviter les fuites. Un premier cathéter est posé pour débuter le rinçage du cerveau avec un mélange de saline et héparine à 38 °C. Au moins 20 ml sont admis par ce cathéter. En



parallèle, la deuxième artère carotide interne est canulée et le rinçage se poursuit avec 40 ml dans chacune des artères. Le rinçage du cerveau conduit petit à petit au décès de l'animal.

Le produit de contraste μ Angiofil (Fumedica AG, Suisse) est préparé suivant les recommandations du fournisseur. Les seringues de durcisseur et polymère sont connectées au mélangeur (*mixing tube*). Celui-ci est généreusement vidangé pour faire sortir toutes les bulles d'air. Il est ensuite raccordé aux deux cathéters pour débuter la perfusion. L'injection se fait manuellement en exerçant une pression assez importante pour contrer la viscosité du produit.

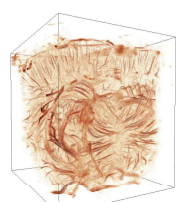
Au cours de la perfusion, la tête, la langue et les yeux deviennent bleu-vert, signe d'une bonne perfusion. Le produit doit alors ressortir par les veines. Pour un cerveau de rat âgé de 7 semaines, environ 6 ml de produit sont injectés.

L'animal est laissé à température ambiante au moins 30 minutes pour la catalyse du polymère. Le moule du vascularisation est alors dur, et le cerveau est ensuite prélevé et fixé dans du paraformaldéhyde.

Deux scanners ont été utilisés pour réaliser la microtomographie du cerveau. D'abord un micro-CT pré-clinique *in vivo* Inveon PET-CT 838 (Siemens, Allemagne), avec une taille de voxel isotrope de 37 μ m. Puis, le même cerveau a été scanné avec un micro-CT *ex vivo* Skyscan 1172 (Bruker microCT, Kontich, Belgique) avec une taille de voxel de 5 μ m et un temps total d'acquisition de 8,5 heures (80 kV, 100 μ A).

3.1.3 Résultats

Les résultats d'imagerie sont présentés dans la figure [fig. 2.10], avec l'imagerie Doppler avec agent de contraste, l'ULM, l'angio-CT (scanner *in vivo*), et le microangio-CT (scanner *ex vivo*). Les images ultrasonores résultent d'une projection en élévation de quelques millimètres d'épaisseur dans le plan devant le transducteur. L'épaisseur de cette projection en élévation n'est pas constante, il est difficile de retrouver parfaitement le même champ de vue dans les volumes 3D.



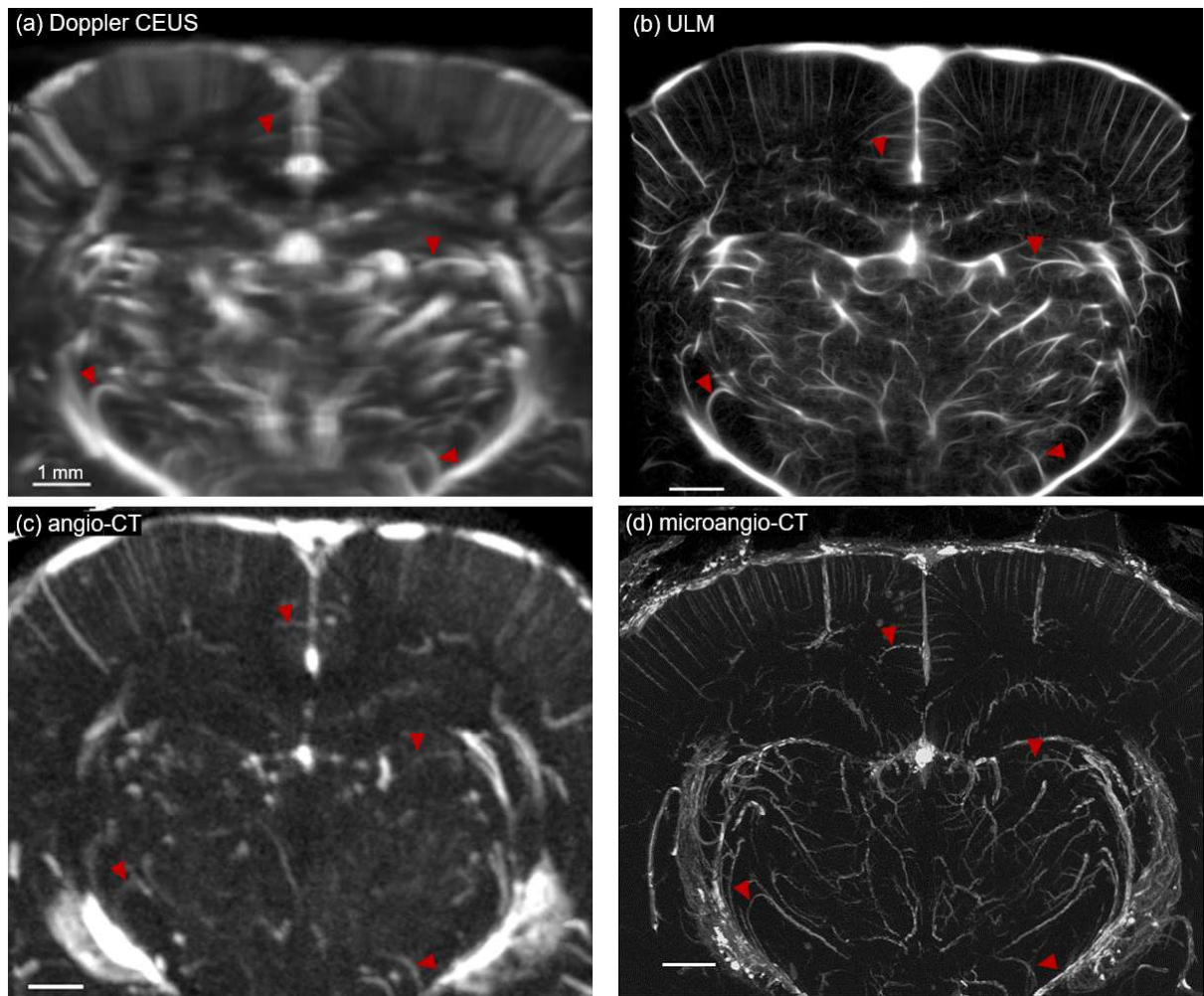
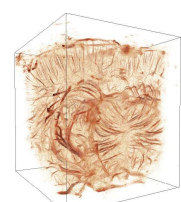


FIGURE 2.10 – Microvascularisation multimodale du cerveau de rat. Imagerie ultrasonore à 15 MHz avec craniectomie : (a) Doppler CEUS, et (b) ULM. Microtomographie aux rayons X avec perfusion d’agent de contraste μ Angiofil (Fumedica) : (c) scanner *in vivo* Inveon PET-CT 838 (Siemens), (d) scanner *ex vivo* Skyscan 1172 (Bruker microCT).

Les structures vasculaires importantes se retrouvent dans toutes les modalités d’imagerie avec des résolutions et contrastes différents. L’imagerie Doppler CEUS, limitée par la diffraction, offre une résolution proche de la longueur d’onde, mais est réalisée *in vivo* en temps réel avec une résolution temporelle très élevée (plusieurs centaines de hertz), et une bonne sensibilité aux flux vasculaires.

Toujours *in vivo*, l’ULM dépasse la limite de diffraction avec une résolution améliorée jusqu’aux petits vaisseaux. Comparée au Doppler, cette modalité nécessite une acquisition de quelques minutes sans mouvements et la perfusion d’agent de contraste.

Les imageries par tomographie aux rayons X sont beaucoup plus compliquées à mettre en place, nécessitant la perfusion d’un agent radio-opaque et le sacrifice de l’animal, et donc la perte de l’information hémodynamique. La microvascularisation apparaît en tout point perfusé d’agent de contraste. Si la perfusion n’est pas parfaite, avec par exemple une bulle d’air obstruant une artère, toute une partie du cerveau peut être absente : l’aval de l’obstruction. Ceci peut



introduire un biais pour l'étude *post-mortem* des ischémies. La sensibilité et le contraste sont très bons pour les gros troncs vasculaires, avec une grande quantité d'agent de contraste. Pour les plus petits vaisseaux, la sensibilité va dépendre de la résolution du système de tomographie et de la taille des voxels reconstruits : plus les voxels sont petits, moins ils sont concentrés en agent radio-opaque et le ratio signal-sur-bruit est diminué.

3.1.4 Conclusion

La comparaison avec l'imagerie par tomographie aux rayons X confirme la faculté de l'ULM à imager les microvaisseaux du cerveau. Les déformations induites par le processus de perfusion, le décès de l'animal, et la fixation empêchent un recalage parfait des volumes acquis *in vivo* et *ex vivo*. Les sensibilités des systèmes ne permettent pas de résoudre précisément le lit capillaire. D'autres techniques comme l'imagerie confocale permettrait cette comparaison sur la couche superficielle du cortex.

3.2 Rendus graphiques pour l'ULM

Le processus de traitement pour l'ULM génère une liste de trajectoire de microbulles, avec leur vitesse en chaque point. Cet ensemble de données parcimonieux n'est pas interprétable par l'utilisateur tel quel pour apprécier la vascularisation d'un organe. Pour rendre compte des densités de vaisseaux, les trajectoires sont accumulées sur une grille, représentant les lieux de passage des microbulles [section 4.2.6]. La taille des pixels est choisie plus petite que celle des images sources avec une amélioration de résolution [[fig. 2.11a-b](#)].

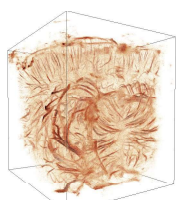
Pour rendre compte des vitesses, on peut utiliser la même grille et moyenner les vitesses de trajectoires pour chaque pixel. Ce type de rendu ne permet cependant pas de prendre en compte le nombre de bulles étant passées par ce pixel : pour une même vitesse moyenne, la valeur sera plus moins erronée s'il y a un grand nombre de valeurs moyennées (avec un écart-type élevé).

On peut alors utiliser un encodage couleur spécifique pour exprimer les différentes informations des trajectoires :

- intensité : nombre de trajectoires traversant le pixel
- vitesse : vitesse moyenne des microbulles dans le pixel
- direction : orientation du vecteur vitesse

L'encodage des pixels est réalisé avec le système colorimétrique *HSL* [[fig. 2.11a](#)] :

- H, *Hue* (teinte) : couleur avec une variation des trois couleurs primaires sur 360°
- S, *Saturation* (saturation) : couleur achromatique, de la couleur vive au gris
- L, *Lightness* (luminosité) : du blanc au noir



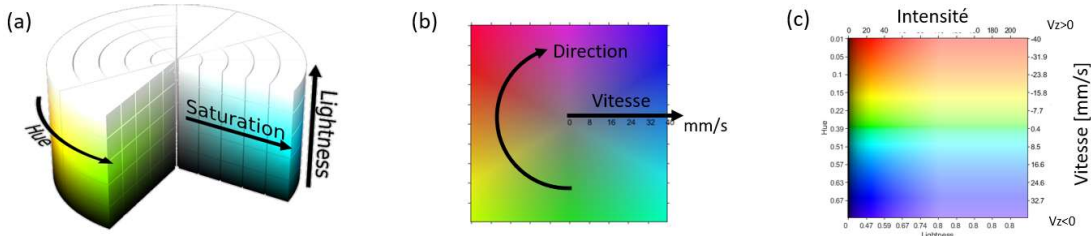


FIGURE 2.11 – (a) Système d’encodage des couleurs HSL (*Hue, Saturation, Lightness*). (b) La direction des flux est associée à la teinte, et la vitesse à la saturation. (c) La vitesse est associée à la teinte, avec une distinction sur le signe de la composante verticale. L’intensité donne la luminosité.

Suivant l’organisation de la microvascularisation dans l’organe, on peut adapter le type de rendu pour aider à la compréhension. Dans le rein [fig. 2.12], l’orientation des petits vaisseaux du cortex est globalement radiale, avec des flux qui vont vers le centre (le bassinet) ou vers l’extérieur. On peut alors choisir d’encoder l’orientation du vecteur vitesse avec la couleur sur 360° , et l’amplitude de la vitesse avec la luminosité [fig. 2.11b].

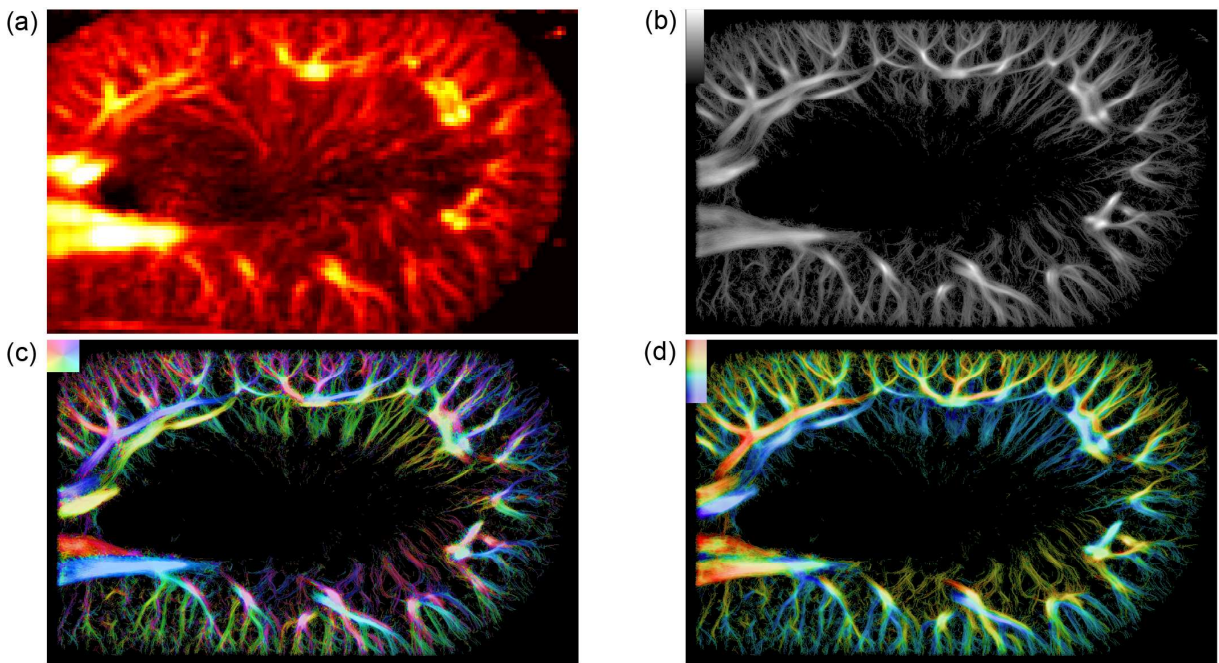
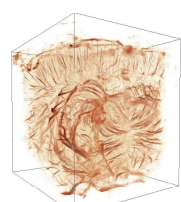


FIGURE 2.12 – Microvascularisation du rein de rat. (a) Doppler ultra-sensible avec agent de contraste. (b) Rendu ULM avec intensité. (c) Rendu avec vitesse (maximum 40 mm/s), encodage couleur de la composante axiale. (d) Rendu vitesse avec encodage couleur de direction.

Pour le cerveau, le cortex présente une architecture plutôt axiale, avec des artères qui descendent dans le cerveau, et des veines qui remontent vers la surface. Dans ce cas, on peut utiliser la couleur pour encoder l’amplitude de vitesse sur une partie restreinte de la teinte, en faisant la distinction sur la composante verticale [fig. 2.11c] : la grandeur $\vec{v} \cdot \vec{u}_z$ fait varier la teinte entre $-v_{max}$ et v_{max} .



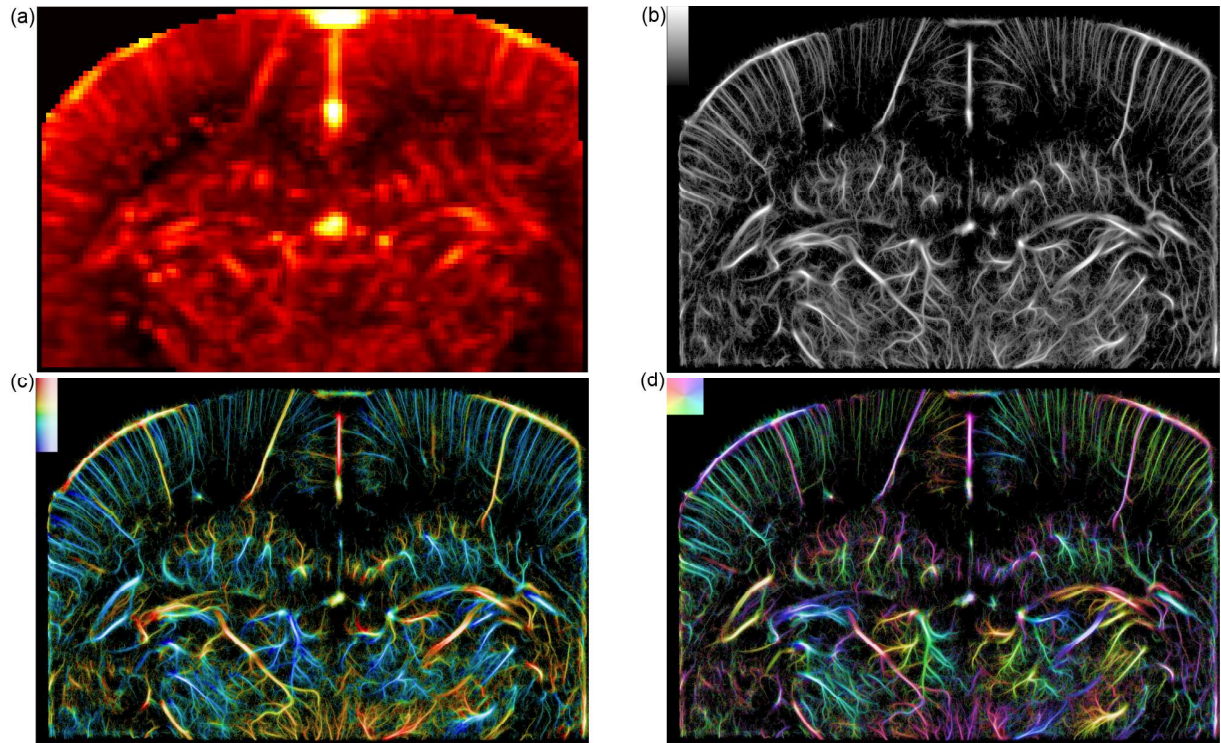


FIGURE 2.13 – Microvascularisation du cerveau de rat avec craniectomie. (a) Doppler ultrasensible avec agent de contraste. (b) Rendu ULM avec intensité. (c) Rendu avec vitesse (maximum 60 mm/s), encodage couleur de la composante axiale. (d) Rendu vitesse avec encodage couleur de direction.

L'utilisation de ce type de rendu graphique facilite la compréhension de données produite par l'ULM en combinant différentes informations des microbulles, leur vitesse, et leur direction.

